

# Stoichiometric Control over Ferroic Behavior in $\text{Ba}(\text{Ti}_{1-x}\text{Fe}_x)\text{O}_3$ Nanocrystals

Julien Lombardi,<sup>†,‡,§</sup> Long Yang,<sup>||</sup> Frederick A. Pearsall,<sup>†,‡,§</sup> Nasim Farahmand,<sup>†,‡,§</sup> Zheng Gai,<sup>⊥</sup> Simon J. L. Billinge,<sup>||,#</sup> and Stephen O'Brien<sup>\*,†,‡,§</sup>

<sup>†</sup>The CUNY Energy Institute, The City College of New York, City University of New York, Steinman Hall, 160 Convent Avenue, New York, New York 10031, United States

<sup>‡</sup>Department of Chemistry, The City College of New York, 1024 Marshak, 160 Convent Avenue, New York, New York 10031, United States

<sup>§</sup>Ph.D. Program in Chemistry, The Graduate Center of the City University of New York, New York, New York 10016, United States

<sup>||</sup>Department of Applied Physics and Applied Mathematics, Columbia University, 500 West 120th Street, New York, New York 10027, United States

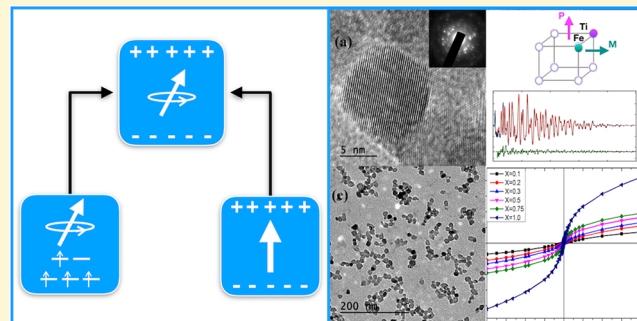
<sup>⊥</sup>Center for Nanophase Materials Sciences and Chemical Science Division, Oak Ridge National Laboratory, Oak Ridge, Tennessee 37831, United States

<sup>#</sup>Condensed Matter Physics and Materials Science Department, Brookhaven National Laboratory, Upton, New York 11973, United States

## Supporting Information

**ABSTRACT:**  $\text{Ba}(\text{Ti},\text{Fe})\text{O}_3$  is a useful system for the exploration of multiferroic properties as a function of composition and variation in structure, based upon a model of intersubstitution of the B site cation. Nanocrystals of  $\text{Ba}(\text{Ti},\text{Fe})\text{O}_3$  could be used as building blocks for composite multiferroic materials, provided ferroic properties are recognizable at this length scale and Ti and Fe serve as ideal models for the case of  $d^0$  versus  $d^n$  in a ferroic perovskite. A series of iron-substituted barium titanate nanocrystals ( $\text{BaTi}_{1-x}\text{Fe}_x\text{O}_3$ ) were synthesized at 60 °C using a hybrid sol-gel chemical solution processing method. No further crystallization/calcination steps were required. The as-prepared nanocrystals are fully crystalline, uniform in size (~8 nm by TEM), and dispersible in polar organic solvents, yielding nanocrystal/alcohol formulations. Complete consumption of the reactant precursors ensures adequate control over stoichiometry of the final product, over a full range of  $x$  (0, 0.1 to 0.75, 1.0). Pair distribution function (PDF) analysis enabled in-depth structural characterization (phase, space group, unit cell parameters, etc.) and shows that, in the case of  $x = 0, 0.1, 0.2, 0.3$ ,  $\text{BaTiO}_3$ , and  $\text{BaTi}_{1-x}\text{Fe}_x\text{O}_3$  nanocrystals, it is concluded that they are tetragonal noncentrosymmetric  $P4mm$  with lattice parameters increasing from, e.g.,  $c = 4.04$  to  $4.08$  Å. XPS analysis confirms the presence of both  $\text{Fe}^{3+}(d^5)$  and  $\text{Fe}^{4+}(d^4)$ , both candidates for multiferroicity in this system, given certain spin configurations in octahedral field splitting. The PDF indicated lattice expansion is attributed to  $\text{Fe}^{3+}(d^5, \text{HS})$  incorporation. The evidence of noncentrosymmetry, lattice expansion, and XPS conformation of  $\text{Fe}^{3+}$  provides support for the existence of multiferroicity in these sub-10 nm uniform dispersed nanocrystals. For  $x > 0.5$ , Fe impacts the structure but still produces dispersible, relatively monodisperse nanocrystals. XPS also shows an increasing amount of  $\text{Fe}^{4+}$  with increasing Fe, suggesting that Fe(IV) is evolving as charge compensation with decreasing  $\text{Ti}^{4+}$ , while attempting to preserve the perovskite structure. A mixture of  $\text{Fe}^{3+}/\text{Fe}^{4+}$  is thought to reside at the B site:  $\text{Fe}^{4+}$  helps stabilize the structure through charge balancing, while  $\text{Fe}^{3+}$  may be complimented with oxygen vacancies to some extent, especially at the surface. The structure may therefore be of the form  $\text{BaTi}_{1-x}\text{Fe}_x\text{O}_{3-\delta}$  for increasing  $x$ . At higher concentrations ( $\text{Fe} > 0.5$ ) the emergence of  $\text{BaFeO}_3$  and/or  $\text{BaFe}_2\text{O}_4$  is offered as an explanation for competing phases, with  $\text{BaFeO}_3$  as the likeliest competing phase for  $x = 1.0$ . Because of the good dispersibility of the nanocrystals in solvents, spin coating of uniform 0–3 nanocomposite  $\text{BaTi}_{1-x}\text{Fe}_x\text{O}_3/\text{polyvinylpyrrolidone}$  thin film capacitors (<0.5 μm) was possible. Frequency dependent dielectric measurements showed stable dielectric constants at 1 MHz of 27.0 to 22.2 for  $\text{BaTi}_{1-x}\text{Fe}_x\text{O}_3$  samples for  $x = 0–0.75$ , respectively. Loss tangent

continued...



Received: October 22, 2018

Revised: January 11, 2019

Published: January 14, 2019

values at 1 MHz were  $\sim$ 0.04, demonstrating the ability to prepare capacitors of magnetic  $\text{Ba}(\text{Ti}_{1-x}\text{Fe}_x)\text{O}_3$  with relatively high permittivity. Magnetic characterization by MPMS (both magnetic hysteresis loops and zero field and field cooling measurements) showed increased magnetization with increasing Fe ion concentration. Weak magnetic coercivity and a small remanence magnetization is observed ( $<5$  K), implying a weak ferromagnetic state at low temperatures ( $<5$  K).

## ■ INTRODUCTION

Materials that exhibit ferroelectric and ferromagnetic (ferroic) properties have attracted the attention of many researchers especially for the multidisciplinary topics of information storage, spintronics, and multiple-state memory storage devices.<sup>1–4</sup> The term multiferroic is used to describe the coexistence of ferroelectricity and ferromagnetism in a single material. Furthermore, a coupling between these two order parameters, termed the magnetoelectric (ME) effect, can potentially enable the control of ferromagnetic behavior by an electric field and vice versa. Materials of these complex orderings are few and far between when it comes to naturally occurring minerals, and fewer still, yet desirable, are those that exhibit ME coupling.<sup>5</sup> A device in which the magnetization is controlled by an electric field, preferably at low voltages, at room temperature and with ultrafast switching, is a prime goal.<sup>6</sup> The added dimensions create multiple possibilities for smart material technology, 4-state logic, and memory solutions for quantum computing. These concepts are being explored extensively, becoming a major field of inquiry.<sup>7,8</sup> A number of novel multiferroic concepts and devices are emerging at this present time.<sup>9,10</sup> The challenge of preparing single phase multiferroics is a stimulating synthetic challenge under continuous revision and exploration,<sup>11,12</sup> and for a while it appeared, in the case of perovskites, that one property could only exist at the exclusion of the other, in the sense that  $d^0$  was an almost necessary requisite for ferroelectricity, while  $d^n$  ( $n > 0$ ) is a necessary requisite for magnetism. When designing a multiferroic material, there are generally two routes to follow: one can layer alternating ferroelectric and ferromagnetic materials,<sup>13–15</sup> or one can aim to design a single phase material by doping a magnetic species into a known ferroelectric material.<sup>16</sup> In the latter case, chemical solution processing via inorganic molecular precursors can potentially offer novel chemical reaction pathways in thermodynamic space, with the goal of isolating new compounds, ease of control over stoichiometry, or difficult to attain phases, when compared to traditional high temperature solid state synthesis frequently used for multiferroics.

The most well studied perovskite ferroelectric metal oxide is  $\text{BaTiO}_3$  due to its versatility in electronic applications, ubiquitous presence in capacitors, and room temperature ferroelectricity.<sup>17</sup> While suppression of the magnitude of ferroelectric polarization is observed in solution processed  $\text{BaTiO}_3$  at the nanoscale, there is strong evidence to support the retention of off-center Ti distortions all the way down to 5 nm, that can be the source of switchable dipoles and ferroelectricity.<sup>18–22</sup> Therefore, it is still of consequence to pursue the development of multiferroic compounds derived from nanoscale  $\text{BaTiO}_3$ , bearing in mind a likely suppression of  $T_c$  and/or more the requirement of sensitive techniques for the detection of potential multiferroic behavior. Synthesis of  $\text{BaTiO}_3$  can be achieved using multiple routes from high temperature solid state syntheses<sup>23</sup> to sol–gel approaches<sup>24</sup> to hydrothermal syntheses.<sup>25</sup> These methods require high temperatures synthesis while low temperature chemical solution processing of nanocrystalline perovskite oxides can ultimately offer thin film integration

options in device electronics for which high temperatures are not suitable. A universal challenge, both in the commercial and in university R&D settings is to develop alternatives to high temperature ceramic processing (firing, sintering or calcination) that can allow for a broader range of ceramic technologies to be integrated more effectively with circuit design and open more technology avenues such as flexible electronics, novel device topologies, and roll-to-roll fabrication.<sup>26–28</sup> This challenge applies to magnetoelectric materials too. Single crystals of  $\text{BaTiO}_3$  that have been doped at the titanium site with  $\text{Fe}^{n+}$  have previously been shown to demonstrate large and recoverable electrostrain of up to 0.8% that is thought to be due to the alignment of  $\text{O}^{2-}$  vacancies with the crystallographic symmetry in the ferroelectric state.<sup>29</sup> It has been postulated that the possibility of Fe incorporation could give rise to multiferroic coupling. In the case of nanostructures, multiferroicism is further proposed to be obtainable due to the large number of superficial atoms that significantly affect bulk behavior. A recent report<sup>30</sup> on the synthesis of aggregate-free single-phase transition-metal-doped  $\text{BaTiO}_3$  quasi-monodisperse cuboidal 15–70 nm nanocrystals follows a synthetic route that allows for the inclusion of magnetic ions such as  $\text{M}^{n+}$  ( $\text{M} = \text{Cr}, \text{Mn}, \text{Fe}, \text{Co}$ ) up to a nominal concentration of 4%, readily detected by EPR and VSM. To probe nanoscale ferroelectricity, the DART-PFM method showed the presence of a hysteretic behavior in the phase signal with a 180° phase shift, as expected from the switching of the dielectric polarization. This is compelling evidence to explore further the effect of transition metal doping on structure and multiferroic behavior in nanoscale  $\text{BaTiO}_3$  over a wide range of compositions.

We previously reported a simple, green, and scalable “self-collection” growth method to produce uniform and aggregate-free colloidal perovskite oxide nanocrystals including  $\text{BaTiO}_3$  (BTO),  $\text{Ba}_x\text{Sr}_{1-x}\text{TiO}_3$  (BST), and  $\text{BaSrTiHfO}_3$  (BSTH) in high crystallinity and high purity.<sup>31</sup> The synthetic method is solution processed, derived from the sol–gel hydrolysis of metal alkoxides in alcohol solvents such as ethanol by stoichiometric amounts of water in the absence of surfactants and stabilizers. The synthesis is performed under an inert nitrogen or argon atmosphere in a glovebox, and the hydrolysis reaction produces nanoscale fully crystallized single domain perovskite metal oxides of the formula  $\text{ABO}_3$  where A and B are transition metals. The nanocrystals were shown to have a passivated surface layer of hydroxyl/alkyl groups, which allows the nanocrystals to exist in the form of a superstable and transparent sol or self-accumulate to form a highly crystalline solid gel monolith (hence “gel-collection”) of 100% yield for easy separation/purification. The dispersibility of the particles in solvents enables the generation of smooth nanocomposite thin films that can be spray printed or spin coated to make single and multilayer capacitors.<sup>32</sup>

In the present work we use a chemical solution technique to synthesize  $\text{BaTiO}_3$  (BTO) as well as  $\text{BaFe}_x\text{Ti}_{1-x}\text{O}_3$  (BFT). Textbook data for crystal ionic radii of the Ti/Fe ions shows that a substitution is geometrically feasible in the 6-coordinate B site (Ti(IV), 74.5; Fe(IV), 72.5 Fe(II), 75(LS), 92(HS); Fe(III), 69 (LS); 78.5(HS), values in pm, *Shannon ionic radii*). The aim of

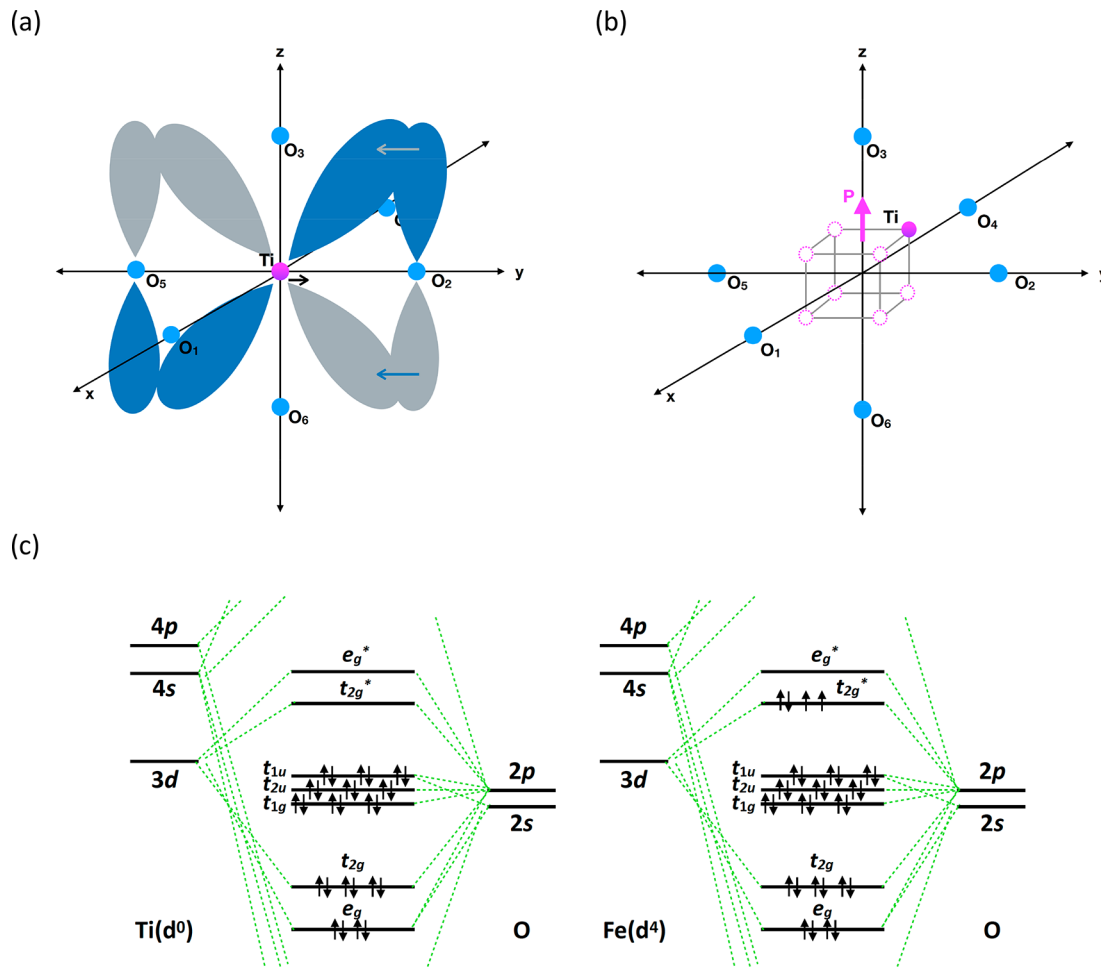


**Figure 1.** Schematic showing (a) overlap of vacant metal d-orbitals with occupied p-orbitals of the oxygen promoting off center distortion of the  $Ti^{4+}$  cation. The displacement of the Ti ion in the  $y$  direction changes the overlap integral to a nonzero value, inducing additional covalence in the Ti–O bonding. (b) PJTE theorem predicts eight equivalent minima (at the corners of a cube in three coordinate space) in which the Ti atom is displaced along the trigonal axes, equally close to three oxygen atoms and removed from the other three. A net average polarization,  $P$ , along [100] is shown to represent the tetragonal phase with two directions of disorder ( $P\uparrow$  and  $P\downarrow$ ) commensurate with room temperature observations. (c) Energy level diagrams and hypothesized occupancies for a  $d^4$  metal, such as  $Fe^{4+}$  (for review with Table 1). Adapted with permission from Bersuker.<sup>37</sup> Copyright 2013 American Chemical Society.

this study was to adapt gel collection<sup>31</sup> to the synthesis of BTO, BFT ( $x = 0.1$ –0.3, 0.5, and 0.75), and BaFeO<sub>3</sub> (BFO), and then investigate the structure and magnetic and dielectric properties of these materials.

**Bonding/Structure in  $BaTi_{1-x}Fe_xO_3$  and the Pseudo-Jan–Teller Effect (PJTE).** The  $(BaTi_{1-x}Fe_xO_3)$  system reviewed here can initially be thought of as a solid solution survey of intersubstitution of Fe for Ti on the B site in BaTiO<sub>3</sub>. However, as we shall see, the structure starts to drift for  $x > 0.3$  and eventually splits into more than one compound. BaTiO<sub>3</sub> is the classic single ferroic ferroelectric perovskite ( $ABO_3$ ). The cubic-tetragonal phase transition is associated with the onset of ferroelectricity in the bulk: a lattice distortion accounts for a permanent dipole in the asymmetric unit cell, which leads to a collective ordering of individual unit cell dipoles to give rise to a remanent polarization. When we question how a series of  $d^0$  cations might affect ferroelectric behavior or how the introduction of  $d^4$  cations (such as  $Fe^{3+}$ ) into the B-site may also introduce magnetic behavior, a more detailed analysis as to the origin of structural instability and the potential for multiferroicity is required. Furthermore, understanding the critical size transition, at which bulk polarization or magnetic

behavior is altered due to particle size, is greatly benefitted by an adequate depth of explanation of the structure–property relationship. A brief discussion follows.

For BaTiO<sub>3</sub>, basic models provide an out-of-center distortion of the octahedral  $Ti^{4+}$  cations on the B site within a cubic perovskite cell to cause an obvious  $\delta+/ \delta-$  linear dipole along a Ti–O bond and a plausible explanation for the shift to a tetragonal unit cell.<sup>33,34</sup> More advanced models combine double-well potentials with valence bond theory in order to optimize the effects of short-range ionic attractions and long-range ordering, to arrive at an adiabatic potential energy surface (APES) to describe phase transition sequences.<sup>34,35</sup> A more complete picture can be obtained through the application of molecular orbital theory, using the pseudo-Jahn–Teller effect (PJTE) to derive the APES. PJTE theory, developed for perovskites by Bersuker,<sup>36,37</sup> combines ground and excited states in vibronic coupling interactions to demonstrate nature's tendency to avoid degeneracy and pseudodegeneracy by symmetry breaking. It can be used to explain ferroelectricity by solving the Hamiltonian for one  $ABO_3$  unit cell with a focus on the octahedral fragment  $BO_6^{8-}$ . When considering the energy level diagram for  $BO_6^{8-}$  and the octahedral field surrounding B,

**Table 1.** Conditions that  $\text{ABO}_3$  Perovskites with the Electronic  $d^n$  Configuration for Ti/Fe as the B Site Cation Possess both Ferroelectric and Magnetic Properties Simultaneously<sup>a</sup>

$d^n$	ion	HOMO, EC, and GS term	LUMO, EC, and LUES term	FE	MM	MF
$d^0$	$\text{Ti}^{4+}$	$(t_{1u})^6, ^1\text{A}_{1g}$	$(t_{1u})^5(t_{2g}\uparrow)^1, ^1\text{T}_{1u}$	yes	no	no
$d^1$	$\text{Ti}^{3+}$	$(t_{1u})^6(t_{2g}\uparrow)^1, ^2\text{T}_{2g}$	$(t_{1u})^5(t_{2g}\uparrow)^2, ^4\text{T}_{1u}$	no	yes	no
$d^4$ , LS	$\text{Fe}^{4+}$	$(t_{1u})^6(t_{2g}\uparrow)^3(t_{2g}\downarrow)^1, ^3\text{T}_{2g}$	$(t_{1u})^5(t_{2g}\uparrow)^3(t_{2g}\downarrow)^2, ^3\text{T}_{1u}$	yes	yes	yes
$d^4$ , HS	$\text{Fe}^{4+}$	$(t_{1u})^6(t_{2g}\uparrow)^3(e_g\uparrow)^1, ^5\text{T}_{2g}$	$(t_{1u})^5(t_{2g}\uparrow)^3(e_g\uparrow)^2, ^7\text{T}_{1u}$	no	yes	no
$d^5$ , LS	$\text{Fe}^{3+}$	$(t_{1u})^6(t_{2g}\uparrow)^3(t_{2g}\downarrow)^2, ^2\text{T}_{2g}$	$(t_{1u})^5(t_{2g})^6, ^2\text{T}_{1u}$	yes	yes	yes
$d^5$ , HS	$\text{Fe}^{3+}$	$(t_{1u})^6(t_{2g}\uparrow)^3(e_g\uparrow)^2, ^6\text{A}_{1g}$	$(t_{1u})^5(t_{2g})^4(e_g\uparrow)^2, ^6\text{T}_{1u}$	yes	yes	yes

<sup>a</sup>EC = electronic configuration, GS = ground state, LUES = lowest ungerade excited state, FE = ferroelectric, MM = magnetic, MF = multiferroic, LS = low-spin, HS = high-spin, IS = intermediate spin;  $(t_{1u})^6 = (t_{1u}\downarrow)^3(t_{1u}\uparrow)^3$ ;  $(t_{1u})^5 = (t_{1u}\downarrow)^2(t_{1u}\uparrow)^3$ ;  $(t_{2g})^6 = (t_{2g}\uparrow)^3(t_{2g}\downarrow)^3$ ;  $(e_g)^4 = (e_g\uparrow)^2(e_g\downarrow)^2$ . Adapted with permission from Bersuker.<sup>36</sup> Copyright 2012 American Physical Society.

the highest occupied molecular orbital (HOMO) is  $t_{1u}/t_{2u}$  etc. (predominantly oxygen 2p in character) and the lowest unoccupied MO (LUMO) is  $t_{2g}^*$  (mostly metal 3d); see Figure 1. The HOMO symmetry representations are  $T_{1u}$ ,  $T_{2u}$ ,  $T_{2g}$ , and  $T_{1g}$  of the octahedral symmetry group, while the LUMO representation is  $T_{2g}$ .

In the cubic perovskite configuration, the HOMO–LUMO terms are orthogonal and do not interact (bonding is  $\sigma$  only). But, off-center displacements of atom B lower the cubic symmetry and make additional orbital overlap nonzero, for example, promoting overlap of the 3d orbital  $|T_{2u}(\text{Ti})_{yz}\rangle$  with neighboring O atoms to create  $\pi$  molecular orbitals. This opportunity for orbital overlap implies additional covalence in Ti–O bonding, providing a driving force for out-of-center distortion, and explains the origin of the local dipolar instability that produces the ferroelectric polarization of the crystal. In inorganic chemistry, it is common to contemplate  $\pi$ -bonds created by overlap between occupied nonbonding d-orbitals and vacant antibonding MOs (backbonding), which strongly influences bond length and molecular geometry. PJTE incorporates first excited state transitions (e.g.,  $t_{1u} \rightarrow t_{2g}$ ) to enable an interpretation of the vibronic coupling to the dipole-active displacements of the central atom. The vibronic theory predicts the ferroelectric phase transitions to be, in essence, of order–disorder type. The trigger mechanism of spontaneous polarization of the crystal is thought to be PJTE in origin, but the magnitude of local distortion and the crystal polarization depend also on the long-range interactions. Ferroelectricity, being directly related to lattice instability, is highly sensitive to B–O bond distances, which can be readily affected by the A atom, as well as an acute dependence on B, both in terms of size and electronic configuration. It is therefore of great interest to inquire both theoretically and experimentally how compositional control can affect electrical/magnetic properties. Progressive treatment of the  $\text{BO}_6^{8-}$  unit is through finding solutions with the introduction of  $d^n$  elements, where  $n > 0$ , for example, when Fe ions are added to the B site, as is the case described here. The  $d^0$  ( $\text{Ti}^{4+}$ ) site is no longer “d-zero”.<sup>38</sup> The implication is that unpaired spins in the perovskite structure could lead to a nonzero magnetic moment, providing conditions for the simultaneous existence of ferroelectricity and magnetism (multiferroicity). The conditions of multiferroicity in  $d^n$  perovskites were previously derived from the pseudo Jahn–Teller effect (PJTE), using the proposition that ferroelectric displacements are triggered by vibronic coupling between ground and excited electronic states of opposite parity but same spin multiplicity.<sup>37</sup> Using the notation HS = high-spin and LS = low-spin, it follows that according to PJTE, only B ions with configurations  $d^3$ -LS,  $d^4$ -LS,  $d^5$ -LS and HS,  $d^6$ -HS,  $d^7$ -HS,  $d^8$ , and

$d^9$  can, in principle, produce multiferroics, provided the criterion of instability is fulfilled. Transition metal ions B with configurations  $d^1$ ,  $d^2$ ,  $d^3$ -HS,  $d^4$ -HS,  $d^6$ -LS,  $d^7$ -LS, and  $d^{10}$  are not expected to produce multiferroics with proper ferroelectricity under this mechanism. The ions,  $\text{Fe}^{4+}$ (LS) and  $\text{Fe}^{3+}$ (both LS and HS) could produce multiferroicity under this mechanism (Table 1).

## EXPERIMENTAL SECTION

**Synthesis.** Barium isopropoxide ( $\text{Ba}(\text{OCH}(\text{CH}_3)_2)$ ) and 2.5% (w/v) iron isopropoxide ( $\text{Fe}(\text{OCH}(\text{CH}_3)_3)$ ) in isopropanol were purchased from Alfa Aesar, titanium isopropoxide ( $\text{Ti}(\text{OCH}(\text{CH}_3)_4)$ ), and polyvinylpyrrolidone (avg. mol wt. 10,000), and 98% furfuryl alcohol was purchased from Sigma-Aldrich. Pure ethanol (200 proof) was purchased from Decon Laboratories, Inc. All chemicals were used without any further purification. The 8 nm  $\text{BaTiO}_3$  nanoparticles were synthesized using the gel collection method<sup>31</sup> under an inert nitrogen or argon atmosphere in a glovebox. Stoichiometric amounts of  $\text{Ba}(\text{OCH}(\text{CH}_3)_2)$  (3.37 mmol or 0.861 g) were added to 40 mL of 200 proof ethanol and magnetically stirred until the powder dissolved (~15 min). Then 1 mL of  $\text{Ti}(\text{OCH}(\text{CH}_3)_4)$  was added to the solution and magnetically stirred for 15 min. A solution of 2 mL of deionized  $\text{H}_2\text{O}$  and 8 mL of 200 proof ethanol was prepared, and then 0.5 mL was added every 10 s and stirred for 5 min after the entire solution was added. The solution was then transferred into a sealed container (e.g., a centrifuge tube with a cap) and left to age overnight in the glovebox. A solid gel rod began to form after 8 h, and the container was transferred out of the glovebox and heated to 60 °C for 12 h for condensation of the gel rod to occur. The gel rod was then washed 3 times with 200 proof ethanol and dried in a vacuum oven overnight at 90 °C in order to be analyzed using X-ray powder diffraction (XRD) and X-ray photoelectron spectroscopy (XPS). Alternatively, the gel rod can be washed and suspended in 200 proof ethanol or furfuryl alcohol (FA) and then spin coated for dielectric measurements.  $\text{BaFe}_x\text{Ti}_{1-x}\text{O}_3$  nanoparticles were synthesized using the same method but with the addition of stoichiometric amounts of  $\text{Fe}(\text{OCH}(\text{CH}_3)_3)$ .  $\text{BaFeO}_3$  nanoparticles were synthesized in the absence of  $\text{Ti}(\text{OCH}(\text{CH}_3)_4)$  using the gel collection method outlined above.

**Characterization.** The resulting  $\text{BaTiO}_3$  (BTO),  $\text{BaFe}_x\text{Ti}_{1-x}\text{O}_3$  (BFT), and  $\text{BaFeO}_3$  (BFO) nanoparticles were characterized using powder X-ray diffraction (XRD), X-ray photoelectron spectroscopy (XPS), transmission electron microscopy (TEM), energy-dispersive X-ray spectroscopy (EDS), scanning electron microscopy (SEM), and magnetic properties measurement system (MPMS). The XRD measurements of the dried BT and BFT powders were performed on a PANalytical X'Pert pro using  $\text{Cu K}\alpha$  radiation. XPS measurements were recorded of the BFT powder samples on a Physical Electronics Versaprobe II XPS. The XPS peaks were fitted using MultiPak v. 9.6.0.15 software. Samples for the TEM were prepared by dispersing the nanocrystalline gel rods (prior to drying in a vacuum oven at 90 °C) in 200 proof ethanol and placing 5  $\mu\text{L}$  of the resulting solution on a carbon coated copper grid. TEM and EDS measurements were recorded on a JEOL 2100 microscope. Magnetic measurements were performed using

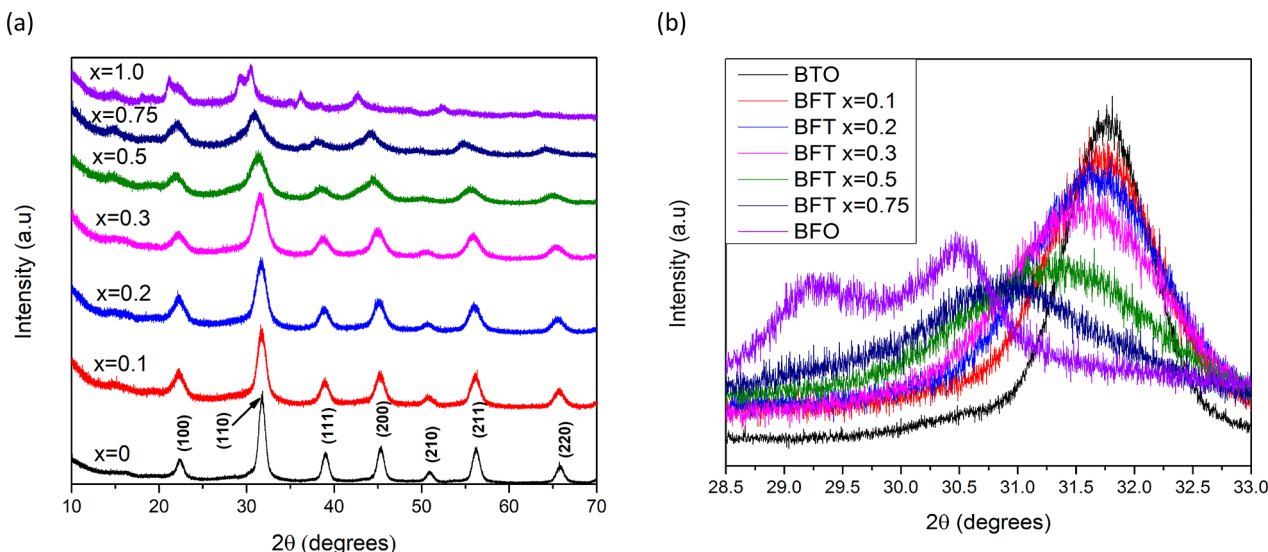


**Figure 2.** (a) X-ray powder diffraction patterns of BTO, BFT ( $x = 0.1\text{--}0.3, 0.5$ , and  $0.75$ ), and BFO. (b) enlargement of the  $(110)$  peak showing a shift in the  $2\theta$  degree indicating a change in lattice parameter.

a Quantum Design Magnetic Property Measurement System (MPMS) at Oak Ridge National Laboratory in Tennessee. The field cooled (FC)–zero field cooled (ZFC) measurements were carried out between the temperature range of  $0\text{--}300$  K. For the ZFC measurement, the sample was cooled in the absence of a field and the magnetization was measured during warming by applying a magnetic field of 2000 Oe. For the FC measurement, the sample was cooled in the presence of a magnetic field of 2000 Oe and the magnetization was measured during cooling under the same field. Magnetic hysteresis loops were measured on the same instrument at 5 K by varying the magnetic field from  $-40\,000$  Oe to  $40\,000$  Oe and measuring the magnetization. In order to study the effect of increasing iron content on the optical properties of each chemical variant, diffuse reflectance UV–vis–NIR (DR UV–vis–NBIR) measurements were performed using a Cary 500 Scan UV–vis–NIR spectrophotometer. Measurements were done over a wavelength range of  $300\text{--}800$  nm.

Impedance analysis was performed on all samples in order to measure the frequency dependent dielectric constant. The  $0\text{--}3$  thin film (450 nm) nanocomposites were prepared in order to determine the effective dielectric constant. The gel rods were dispersed in ethanol, and the resulting solution was spin coated onto thermally evaporated electrodes (evaporated using a Denton Vacuum LLC Benchtop Turbo) on a silicon or glass substrate. A solution of 20 mg/mL polyvinylpyrrolidone (PVP) dispersed in ethanol was spin coated on top of the thin film of nanoparticles in order to fill the void space between nanoparticles and make a  $0\text{--}3$  nanocomposite. The resulting film was heated to  $90$  °C for 6 h in order to evaporate all solvents. A top electrode was then thermally evaporated covering a cross section of  $1\text{ mm}^2$  on the film, and the capacitor was probed over the frequency range of  $100$  Hz– $2$  MHz in order to measure the capacitance and dielectric loss tangent using an Agilent E4980A Precision LCR Meter. Cross sectional SEM samples of the  $0\text{--}3$  nanocomposites were prepared by freeze cracking the nanocomposite thin films with liquid nitrogen. The SEM micrographs were recorded on a Supra 55 SEM.

## RESULTS AND DISCUSSION

**Part I: Structural, Spectroscopic, and Optical Characterization of  $\text{BaTi}_{1-x}\text{Fe}_x\text{O}_3$  Nanocrystals.** BTO, BFT ( $x = 0.1\text{--}0.3, 0.5$ , and  $0.75$ ), and BFO nanocrystals were synthesized using the gel collection method. Gel collection employs a treatment of reactive alkoxide precursors that are initially reacted under an inert atmosphere ( $\text{N}_2$  or Ar) in the absence of oxygen/moisture. Following formation of a homogenized solution, in which precursors have coreacted, stoichiometric

levels of deionized water are used to initiate hydrolysis and further promote polycondensation, using a low temperature ( $60$  °C) heating step. All of the reactants are consumed and collected as the product, which insures that the reactant stoichiometry input is equivalent in molarity output. It can therefore be assumed that a reaction with a specific molar ratio (e.g.,  $x = 0.3$ ) will yield a defined product (e.g.,  $\text{BaTi}_{0.7}\text{Fe}_{0.3}\text{O}_3$ ), later confirmed by structural and spectroscopic characterization. The synthesized nanoparticles are crystallized and readily dispersed in polar organic solvents, suitable for preparing thin films. X-ray powder diffraction can confirm phase and, to a large extent, phase purity. The powder diffraction patterns are shown in Figure 2. The sample quantity was more than sufficient for powder XRD ( $>200$  mg), but even at long acquisition times, it is evident (Figure 2) that the effects of nanoscale size greatly affect the X-ray powder spectra: such small-scale objects, with a finite number of unit cells and therefore limited intensity range for coherent X-ray scattering based upon Bragg reflection planes, will not provide sharply defined Bragg peaks of high intensity. The use of PDF was therefore highly favored and is explained in detail in Part II, while the following primary observations from powder scattering are noted. The nanocrystals appear to be single phase in the case of lower doping concentrations of Fe. The peak broadening due to particle size is evident, and the Scherrer equation confirms particle sizes  $< 10$  nm ( $\sim 8$  nm, see TEM). For X-ray powder diffraction, peak broadening obscures further structural information, for example, determination of space group, detail on unit cell parameters, phase purity, etc. Ongoing from the pure BTO toward higher Fe content, there is a decrease in intensity and a broadening of the  $(110)$  peak, which results in a lower signal-to-noise in the data. As we discuss later in the detailed PDF analysis of the structure, this results primarily from a decrease in the structural coherence, the emergence of additional phases, and the lower symmetry of the BFO product. However, the peak shift of the  $(110)$  peak is visibly evident (Figure 2b) and can be, to a first approximation, seen to be causing an expansion of the lattice constant. The lattice expansion with increasing quantities of Fe is a good indication of Fe incorporation into the lattice; however, the peak broadening as a consequence of nanocrystal size ( $< 10$  nm) prevents a sound conclusion as to the space group (whether

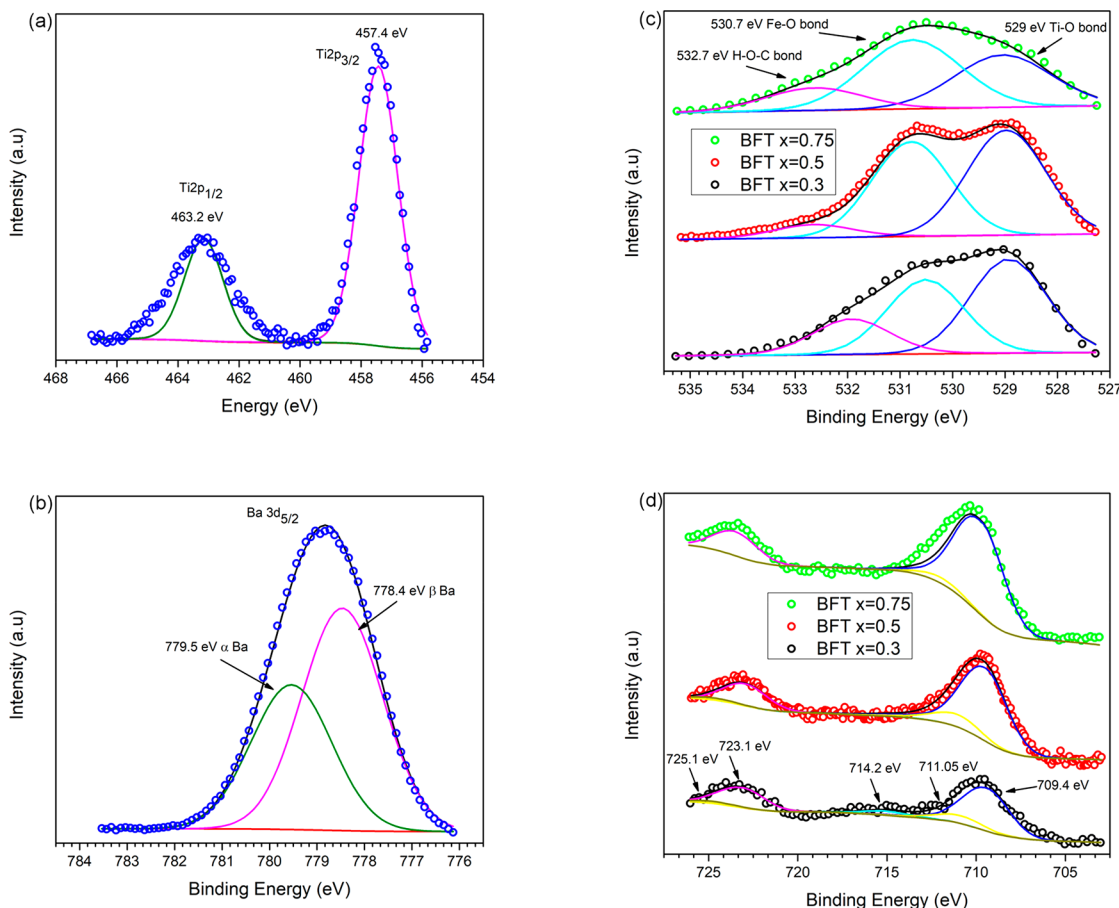


**Figure 3.** XPS spectra of nanocrystalline BFT,  $x = 0.3, 0.5$ , and  $0.75$ : (a) Ti 2p lines of BFT  $x = 0$ , (b) Ba 3d<sub>5/2</sub> lines of BFT  $x = 0.5$ , (c) O 1s lines of BFT  $x = 0.3, 0.5$ , and (d) Fe 2p lines of  $x = 0.3, 0.5$ , and  $0.75$ .

cubic/tetragonal etc.). Furthermore, there is a clear change of phase between  $x = 0.75$  ( $\text{BaTi}_{0.25}\text{FeO}_{0.75}\text{O}_3$ ) and  $x = 1$  ( $\text{BaFeO}_3$ ). The occurrence of the phase change, and a deeper investigation into the lattice parameters for these materials at the nanoscale, warranted advanced structural characterization to be undertaken, using pair distribution function analysis.

Characterization of the valence state of the ions of Fe, Ti, and Ba in BFT  $x = 0.3, 0.5$ , and  $0.75$  samples along with the chemical compositions were obtained by the use of X-ray photoelectron spectroscopy (XPS). The XPS peaks were analyzed and fitted using MultiPak v. 9.6.0.15 software. All spectra presented are from a surface analysis survey and referenced to the C 1s-signal at 284.8 eV. A broad Ba 3d<sub>5/2</sub> peak was observed in the 777–783 eV range and was fitted to two peaks at 779.5 and 778.4 eV, respectively, as shown in Figure 3b, and agree well with features of other  $\text{BaTiO}_3$  solids.<sup>39,40</sup> The deconvolution of the Ba 3d<sub>5/2</sub> peak shows a  $\alpha$ -bulk and  $\beta$ -surface species of  $\text{Ba}^{2+}$ , respectively, as  $\text{Ba}^{2+}$  is in a different chemical environment depending on if it is within the nanoparticle or on the surface. The  $\alpha$  peak is at 779.5 eV, and the  $\beta$  peak is at 778.4 eV; these agree well with prior work as well as with literature.<sup>41,42</sup> Two Ti 2p peaks are present, the Ti 2p<sub>3/2</sub> at 457.4 eV and the Ti 2p<sub>1/2</sub> at 463.2 eV as shown in Figure 3a. These values agree well with literature<sup>39,40</sup> and indicate that the chemical valence of Ti in the range of composition for BFT samples remains the same at  $\text{Ti}^{4+}$ . The Fe 2p lines were fit to five peaks as shown in Figure 3d. The peaks centered at 709.4 and 723.1 eV corresponding to the Fe 2p<sub>3/2</sub> and Fe 2p<sub>1/2</sub>, respectively, agree well with  $\text{Fe}_2\text{O}_3$  spectra in

literature<sup>43</sup> corresponding to the presence of  $\text{Fe}^{3+}$ . The Fe 2p<sub>3/2</sub> peak and the Fe 2p<sub>1/2</sub> peaks were fit to two smaller peaks at 711.05 and 725.1 eV, respectively, corresponding to a small presence of  $\text{Fe}^{4+}$  ions, indicating that the samples of higher iron concentration ( $x \geq 0.3$ ) have a mixed valence of  $\text{Fe}^{3+}$  and  $\text{Fe}^{4+}$  ions in the crystal lattice.<sup>40</sup> The peak at 714.2 eV is a satellite peak that is commonly seen in Fe 2p XPS spectra.<sup>43</sup> The O 1s peak shown in Figure 3d has a main peak centered at 529 eV and two shoulders that appear at 530.7 and 532.7 eV. The three spectra of increasing iron content ( $x = 0.3, 0.5$ , and  $0.75$ ) in Figure 3c show an increase in intensity of the shoulder peak at 530.7 eV as a function of increasing iron content and are thought to correspond to the increase in the amount of Fe–O bonds. A supporting trend in the 529 eV peak of the O 1s spectra is seen as the peak decreases at  $x = 0.75$  iron concentration, indicating that there are now fewer Ti–O bonds than Fe–O bonds which agrees with the stoichiometry. The shoulder at 532.7 eV could be attributed to ethanol groups on the surface of the nanoparticles as well as absorption of  $\text{H}_2\text{O}$  on the surface of the sample. We conclude that XPS analysis confirms the presence of both  $\text{Fe}^{3+}(d^5)$  and  $\text{Fe}^{4+}(d^4)$ , both candidates for multiferroicity in this system, given low spin configurations in octahedral field splitting. XPS also shows an increasing amount of  $\text{Fe}^{4+}$  with increasing Fe, suggesting that Fe(IV) is evolving in order to account for charge compensation with decreasing quantities of  $\text{Ti}^{4+}$ , while still attempting to preserve the perovskite structure.

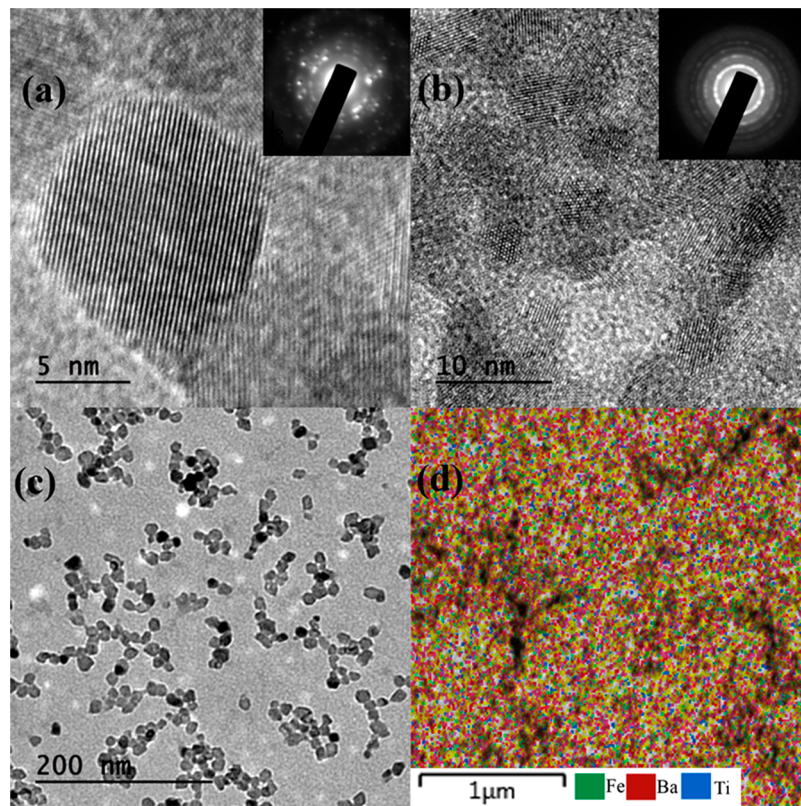


**Figure 4.** TEM images of BFT nanocrystals: (a) HRTEM lattice image of  $\text{BaTi}_{0.9}\text{Fe}_{0.1}\text{O}_3$ , (b) typical HRTEM of BFT,  $x = 0.2, 0.3$ , showing lattice images of multiple nanocrystals, (c) typical lower resolution image of a sample batch of  $\text{BaTi}_{1-x}\text{Fe}_x\text{O}_3$  showing size control, a narrow size distribution  $<10 \text{ nm}$ , and an average size of 8 nm, and (d) EDS elemental mapping showing uniform distribution of Fe, Ba, and Ti ions.

It is clear that  $\text{Fe}^{3+}$  is present from the XPS data, and this agrees with the XRD and PDF data, showing a clear shift in  $2\theta$  corresponding to an increase in lattice parameters. It is concluded from XPS, and further discussed in Part II, that the increase in lattice parameters with the increase in the concentration of Fe corresponds to a doping of  $\text{Fe}^{3+}$  on the  $\text{Ti}^{4+}$  site within the crystal lattice. A mixture of  $\text{Fe}^{3+}/\text{Fe}^{4+}$  ends up residing at the B site:  $\text{Fe}^{4+}$  helps stabilize the structure through charge balancing, while  $\text{Fe}^{3+}$  can be complimented with oxygen vacancies to some extent. Eventually, with increasing Fe ( $x > 0.5$ ), neither  $\text{Fe}^{3+}$  nor  $\text{Fe}^{4+}$  can maintain the structure, and the emergence of more thermodynamically stable Ba–Fe–O phases start to emerge.

Size and morphology of the nanoparticles were confirmed using a JEOL 2100 TEM. As noted earlier, the nanoparticles disperse well in ethanol and other alcohols such as furfuryl alcohol without any use of surfactants. TEM micrographs in Figure 4 confirm that the nanoparticles are uniform in shape and size. The nanoparticles are 8 nm in diameter and spherical in shape across all doping of Fe into the unit cell. Selected area diffraction confirms that the samples are all polycrystalline. EDS mapping (Figure 4d, see also Supporting Information Figure S1) was performed in order to analyze the composition gradient of Fe within the unit cell. The mapping shows that Fe is dispersed evenly throughout the nanoparticles in all the same locations that  $\text{Ba}^{2+}$  and  $\text{Ti}^{4+}$  ions were.

The UV-vis diffuse reflectivity spectra of BTO and BFT,  $x = 0.1–0.3, 0.5, 0.75$ , and 1.0, were measured using a Cary 500 Scan UV-vis–NIR spectrophotometer and are shown in Figure 5 below. The bandgaps of all samples are estimated to be 3.25, 3.09, 2.68, 2.61, 2.5, 2.2, and 1.85 for BTO and BFT,  $x = 0.1–$

0.3, 0.5, 0.75, and 1.0, respectively. The bandgaps ( $E_g$ ) were estimated through extrapolation of the linear fits of Tauc plots versus the photon energy (Supporting Information S2), relying on Kubelka–Munk theory.<sup>44–46</sup> BTO shows an absorption profile with a sharp absorption edge at  $\sim 350 \text{ nm}$  which agrees well with literature.<sup>47</sup> However, upon addition of Fe at varying concentrations, the absorption profile changes as the samples absorb over a broader range from 350 to 600 nm. This difference in absorption profile is reflected in the range of bandgaps ( $E_g$ ). This is no doubt due to the  $\text{Fe}^{3+}$  incorporation in the crystal lattice. Optical absorption is observed in BTO-based oxides due to the transition from the O 2p valence band to the Ti 3d conduction band. This absorption is shifted to longer wavelengths in the case of Fe substitution on the Ti site in the crystal lattice because it creates O vacancies and contributes more d electrons overall which creates overlapping absorption regions resulting in a narrower bandgap.<sup>48</sup>

**Part II: Advanced Structural Characterization of  $\text{BaTi}_{1-x}\text{Fe}_x\text{O}_3$  Nanocrystals: Pair Distribution Function Analysis (PDF).** The iron doped  $\text{BaFe}_x\text{Ti}_{1-x}\text{O}_3$  gel-collected perovskite nanoparticles were studied using X-ray pair distribution function (PDF) analysis<sup>49–56</sup> at room temperature, over the full range of compositions ( $x = 0, 0.1, 0.2, 0.3, 0.5, 0.75, 1.0$ ). PDF is an excellent way to resolve structure at the nanoscale and can take into account exact particle diameters when performing structural refinement for a specific space group, symmetry, and site occupancy. We sought to (a) determine whether these samples have a noncentrosymmetric structure; (b) confirm that Fe was being incorporated into the structure; and (c) look for any structure changes with increased Fe content. Compounds were labeled BTO ( $\text{BaTiO}_3$ ) and

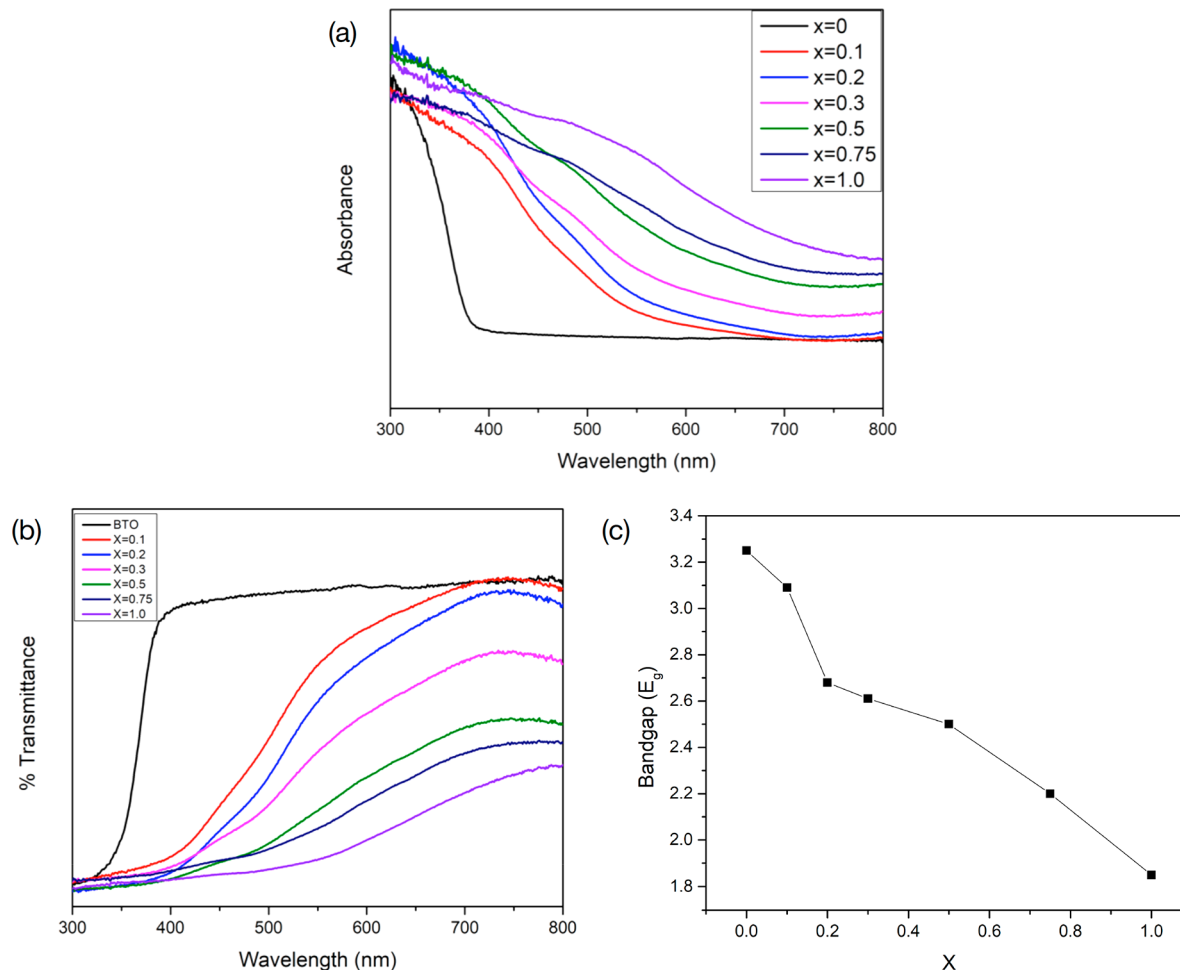


**Figure 5.** Diffuse reflectance spectra of BTO ( $x = 0$ ) and BFO ( $x = 0.1–0.3, 0.5, 0.75$ , and  $1.0$ ): (a) absorbance, (b) % transmittance, and (c) plot of calculated bandgap vs value of  $x$  for all samples.

BFT $x$ , where  $x$  = the composition of Fe, e.g., BFT2 represents BaFe<sub>0.2</sub>Ti<sub>0.8</sub>O<sub>3</sub>. For  $x = 1.0$ , the initial assumption was the compound is BFO, BaFeO<sub>3</sub>. PDF was selected for structural refinement based on the uniform and consistent nanoscale crystallite size (8 nm), which results in extreme Bragg peak broadening (Figure 2). In this crystallite size domain, PDF is generally more accurate than Rietveld or Le Bail for obtaining structural parameters<sup>49,50,57</sup> and often yields quantitative structural information about subnanometer atomic length scale to give comparable or improved lattice parameters.

**PDF Experimental methods.** The X-ray total scattering measurements on these iron doped BaFe <sub>$x$</sub> Ti<sub>1– $x$</sub> O<sub>3</sub> ( $x = 0, 0.1, 0.2, 0.3, 0.5, 0.75, 1.0$ ) samples were carried out at the XPD beamline (28-ID-2) at the National Synchrotron Light Source II (NSLS-II), Brookhaven National Laboratory. The nanocrystalline powders were sealed in polyimide capillaries, and the data were collected at room temperature using the rapid acquisition PDF method (RAPDF).<sup>51</sup> The experimental setup was calibrated by measuring the crystalline nickel as a standard material. A large area 2D PerkinElmer detector was mounted behind the samples with a sample-to-detector distance of 202.80 mm. The incident X-ray wavelength was  $\lambda = 0.1867 \text{ \AA}$ . The instrument resolution is explained by two parameters in modeling,  $Q_{\text{damp}}$  and  $Q_{\text{broad}}$ ,<sup>53,58</sup> which were determined as  $Q_{\text{damp}} = 0.037 \text{ \AA}^{-1}$  and  $Q_{\text{broad}} = 0.017 \text{ \AA}^{-1}$  by fitting the PDF from a well crystallized sample of Ni.

The detector exposure time was 0.1 s for all the samples to avoid detector saturation, and the number of frames taken for the sample was adjusted to be 1200 for sufficient counting statistics on the data, so the total exposure time per sample was 120 s. The collected data frames were summed, corrected for polarization effects, and masked to remove outlier pixels before being integrated along arcs of constant  $Q$ , where  $Q = 4\pi \sin \theta / \lambda$  is the magnitude of the momentum transfer on scattering, to produce 1D powder diffraction patterns using the Fit2D program. Standardized corrections and normalizations were then applied to the data to obtain the total scattering structure function,  $F(Q)$ , which was Fourier transformed to obtain the PDF, using PDFgetX3<sup>52</sup> within xPDFsuite.<sup>59</sup> The maximum range of data used in the Fourier transform was chosen to be  $Q_{\text{max}} 24.0 \text{ \AA}^{-1}$ , so as to give the best trade-off between statistical noise and real-space resolution. For consistency, all PDFs were transformed with the same settings.

The PDF modeling program PDFgui was used for structure refinements. In these refinements  $U_{\text{iso}}$  ( $\text{\AA}^2$ ) is the isotropic atomic displacement parameter (ADP), and in multiphase fits, the ADPs of the same type of atoms are constrained to be the same in different phases;  $\delta_1$  ( $\text{\AA}$ ) is a parameter that describes correlated atomic motions;<sup>60</sup> SPD ( $\text{\AA}$ ) is a parameter that accounts for the finite size of the particle, or more correctly, the domain of coherent scattering in the particle, which gives the diameter of the domain in angstrom units, assuming it to be

**Table 2.** Summary of Structural Models Used for BaTiO<sub>3</sub> Fitting Procedures

	model name				
	CC	CT	NT	NR	NO
crystal system	cubic	tetragonal	tetragonal	rhombohedral	orthorhombic
centrosymmetric	yes	yes	no	no	no
space group	<i>Pm</i> <sup>3</sup> <i>m</i>	<i>P</i> 4/ <i>mmm</i>	<i>P</i> 4 <i>mm</i>	<i>R</i> 3 <i>m</i>	<i>A</i> mm2
Ba position	(0, 0, 0)	(0, 0, 0)	(0, 0, 0)	(0, 0, 0)	(0, 0, 0)
Ti position	(0.5, 0.5, 0.5)	(0.5, 0.5, 0.5)	(0.5, 0.5, <i>z</i> )	( <i>z</i> , <i>z</i> , <i>z</i> )	(0.5, 0, <i>z</i> )
O1 position	(0.5, 0.5, 0)	(0.5, 0.5, 0)	(0.5, 0.5, 0)	( <i>x</i> , <i>y</i> , <i>x</i> )	(0, 0, <i>z</i> )
O2 position		(0.5, 0, 0.5)	(0.5, 0, 0.5)		(0.5, <i>y</i> , <i>z</i> )

spherical.  $Q_{\text{damp}}$  and  $Q_{\text{broad}}$  were refined to a nickel data set collected under the same experimental conditions and then fixed in the nanoparticle refinements. Five candidate BaTiO<sub>3</sub> perovskite models were fit to the experimental PDFs to determine the structure of the gel nanoparticles. All the structure models, based on the perovskite structure of BaTiO<sub>3</sub>, are defined in detail in Table 2.<sup>61</sup>

The NT model was extended for the samples that have iron incorporated in them. Designated NT-BFTO, this model (space group: *P*4*mm*) is built from the NT model by substituting Fe into the Ti site, with variable occupancies on the Fe and Ti sites constrained to keep the total site occupancy as 1.0. The atomic positions and ADPs of Fe and Ti ions are constrained to be the same as each other during the refinement, i.e.,  $z(\text{Ti}) = z(\text{Fe})$  and  $U_{\text{iso}}(\text{Ti}) = U_{\text{iso}}(\text{Fe})$ . We found evidence for a BaCO<sub>3</sub> impurity phase and modeled it with the following orthorhombic (BCO) model (space group: *Pmcn*): with Ba at (0.25, *y*, *z*), C at (0.25, *y*, *z*), O1 at (0.25, *y*, *z*), and O2 at (*x*, *y*, *z*).<sup>62</sup> When using the BCO model as an impurity phase in two-phase fits for BaFe<sub>x</sub>Ti<sub>1-x</sub>O<sub>3</sub> data sets, the ADP of the C ion is fixed as  $U_{\text{iso}}(\text{C}) = 0.04007 \text{ \AA}^2$ , and atomic positions of all atoms were fixed as Ba at (0.25, 0.4164, 0.7544), C at (0.25, 0.7556, -0.0783), and O, O1 at (0.25, 0.9011, -0.0894) and O2 at (0.4601, 0.6832, -0.0820), where these numbers were taken from ref 63.  $\delta_1$  and SPD parameters are not applied during the refinement since the impurity BCO component is too short-range to get stable fitting results. For high Fe content samples, we also used the cubic perovskite BaFeO<sub>3</sub> (BFO) model (space group: *Pm*<sup>3</sup>*m*)<sup>64</sup> with Ba at (0, 0, 0), Fe at (0.5, 0.5, 0.5), and O at (0.5, 0.5, 0); the orthorhombic BaFe<sub>2</sub>O<sub>4</sub> (BF2O4) model (space group: *Pmcn*)<sup>65</sup> with Ba1,2 at (0.25, *y*, *z*), Ba3 at (*x*, *y*, *z*), Fe1,2,3,4 at (*x*, *y*, *z*), O1–7 at (*x*, *y*, *z*), and O8,9 at (0.25, *y*, *z*).

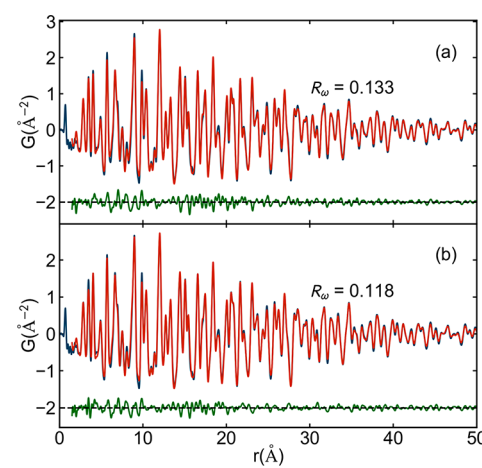
**PDF Results and discussion.** BaTiO<sub>3</sub>. We first considered undoped pristine BTO 8 nm nanocrystals, with the goal of determining whether or not they existed with a centrosymmetric or noncentrosymmetric structure. This would provide evidence for whether a symmetrical cubic (paraelectric) or nonsymmetrical (e.g., tetragonal, ferroelectric) phase can be retained at this length scale in nanocrystals (the 0D case) and provide further insight into the processing–structure–ferroelectric property relationship in nanoscale BaTiO<sub>3</sub>, a topic that has fascinated the community for many years.<sup>66,67</sup>

Following refinement, all five of the perovskite models fit reasonably well. The refinement results are given in Table 3, and representative fits are shown in Figure 6. The centrosymmetric models gave comparable agreements as each other ( $R_w = 0.133$ ) but slightly worse than the N (noncentrosymmetric) models ( $R_w \sim 0.115$ ). There is clearly an indication that the nanocrystals are presenting as noncentrosymmetric. Evidence of tetragonality in BaTiO<sub>3</sub> at comparable length scales (but different processing conditions) has been observed previously.<sup>21</sup>

**Table 3.** Structure Refinement Results of All Candidate Perovskite Models Fit to the BaTiO<sub>3</sub> Data Set over a Range of  $1.5 < r < 50 \text{ \AA}$ <sup>a</sup>

	model				
	CC	CT	NT	NR	NO
$R_w$	0.133	0.133	0.118	0.119	0.115
$a (\text{\AA})$	4.0246	4.0211	4.0170	4.0254	4.0147
$b (\text{\AA})$	-	-	-	-	5.6863
$c (\text{\AA})$	-	4.0318	4.0424	-	5.7141
$\alpha (\text{deg})$	90	90	90	89.795	90
Ba <i>z</i>	-	-	-0.0011	0.0046	-0.0039
Ti <i>z</i>	-	-	0.5328	0.4834	0.5218
O1 <i>x</i>	-	-	-	0.0125	-
O1 <i>z</i>	-	-	-0.0180	0.5157	0.4644
O2 <i>y</i>	-	-	-	-	0.2695
O2 <i>z</i>	-	-	0.4756	-	0.2479
Ba $U_{\text{iso}} (\text{\AA}^2)$	0.0083	0.0082	0.0083	0.0085	0.0086
O $U_{\text{iso}} (\text{\AA}^2)$	0.0287	0.0284	0.0255	0.0264	0.0204
Ti $U_{\text{iso}} (\text{\AA}^2)$	0.0177	0.0176	0.0099	0.0088	0.0087
$\delta_1 (\text{\AA})$	1.44	1.43	1.57	1.55	1.71
SPD ( $\text{\AA}$ )	120.0	122.1	132.4	126.4	129.77

<sup>a</sup>The models are centrosymmetric-cubic (CC), centrosymmetric-tetragonal (CT), non-centrosymmetric-tetragonal (NT), non-centrosymmetric-rhombohedral (NR), and noncentrosymmetric-orthorhombic (NO). Here  $R_w$  is the goodness of fit; *x*, *y*, and *z* are the refinable atomic positions in fractional coordinates (see Table 2 for details),  $U_{\text{iso}}$  (units of  $\text{\AA}^2$ ) is the isotropic atomic displacement parameter (ADP);  $\delta_1$  (units of  $\text{\AA}$ ) is a correlated motion related PDF peak sharpening coefficient; SPD (units of  $\text{\AA}$ ) is the spherical particle diameter.

**Figure 6.** X-ray PDFs of BaTiO<sub>3</sub> (BTO) (blue curves) with the best-fit calculated PDFs (red) for the (a) CC and (b) NT models.

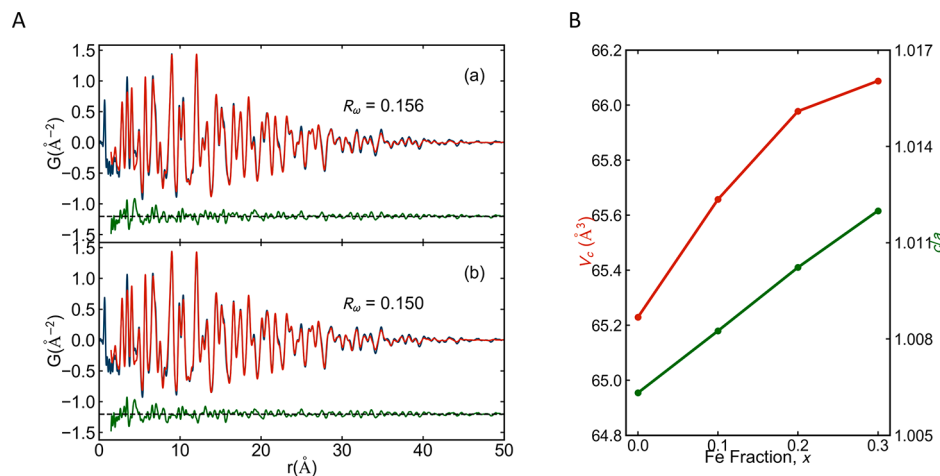


**Figure 7.** A: X-ray PDFs of the BFT3 data (blue curves) with the best-fit calculated PDFs (red) for the (a) NT-BFTO and (b) NT-BFTO + BCO two-phase models. The difference curves are shown offset below in green.  $R_w$  is the goodness of fit. B: Unit cell volume (red curve) and  $c/a$  ratio (green curve) from the NT model as a function of Fe doping concentration  $\text{BaTi}_{1-x}\text{Fe}_x\text{O}_3$  ( $x \leq 3$ ) of samples in the two-phase fits.

Concluding that the underlying structures are noncentrosymmetric based on  $R_w$  alone is insubstantive, because noncentrosymmetric models have more variables. However, strikingly, the Ti atoms refine to values away from the center of symmetry in all the noncentrosymmetric models, and the ADPs of the Ti ions are significantly smaller, in the noncentrosymmetric models compared to the centrosymmetric models, providing further evidence that the underlying structure has Ti off the (0.5, 0.5, 0.5) center of symmetry. This experimental observation is consistent with predictions of the pseudo-Jahn–Teller effect being the underlying cause of off-center displacements of atom B (the Ti atom), lowering the symmetry in order to make additional orbital overlap, between the 3d orbital  $|T_{2u}(\text{Ti})_{yz}\rangle$  and neighboring O atoms to create  $\pi$  molecular orbitals.<sup>37</sup> We also note that the ADPs of the Ba and O ions are comparable between the noncentrosymmetric and centrosymmetric models, which again suggests that the main difference is that the Ti atom is moving off the center of symmetry and that the data strongly support the fact that the nanoparticles are noncentrosymmetric. While noncentrosymmetry can be concluded, the fits for tetragonal ( $P4/mmm$ ), rhombohedral ( $R\bar{3}m$ ), and orthorhombic ( $Amm2$ ) space groups are equally possible. For barium titanate, vibronic theory<sup>37</sup> predicts a ferroelectric ordering with correlated displacement of Ti atoms along the same trigonal direction, [111], corresponding to the rhombohedral phase. But, with increasing thermal excitation in the system it can average over two nearest-neighbor wells, say, [111] and [111̄], by hopping or tunneling yet still be separated from other equivalent pairs by a tetragonal potential barrier that is higher in energy. The crystal is disordered along one of its symmetry axes, remaining ordered along the other two. At the average, the crystal is polarized along [110]. Macroscopically, this type of ordering is equivalent to the orthorhombic phase. Finally, at higher temperatures, the crystal transforms into the tetragonal phase with two directions of disorder polarized, in average, along [100]. We conclude that the results of PDF analysis are consistent with (a) the observation of noncentrosymmetry in BTO nanocrystals and (b) the conclusion that the tetragonal phase is the likeliest candidate structure for RT BTO nanocrystals, based upon a thermal averaging of the orthorhombic phase, which is in turn a thermal average of the rhombohedral phase.

$\text{BaTi}_{1-x}\text{Fe}_x\text{O}_3$  ( $x \leq 3$ ). To verify Fe incorporation into the BTO lattice in the doped  $\text{BaFe}_x\text{Ti}_{1-x}\text{O}_3$ , we fit the NT model, with Fe substituted onto the Ti site (we refer to this as the NT-BFTO model (see modeling) to the low doped  $\text{BaFe}_x\text{Ti}_{1-x}\text{O}_3$  ( $x = 0.1, 0.2, 0.3$ ) data sets. The fits are satisfactory; a representative fit of the BFT3 sample PDF with the NT-BFTO model is shown in Figure 7a. However, following the observation of  $\text{BaCO}_3$  in the higher-doped samples we looked for its presence in these samples by adding it as a second phase to these refinements, i.e., the NT-BFTO+BCO model (Figure 7b). This led to a small improvement in the goodness-of-fit,  $R_w$ , and it might be concluded that trace  $\text{BaCO}_3$  is also present at lower Fe doping concentrations. Barium carbonate (BCO) is known to occur in barium containing oxides in which exposure to atmospheric  $\text{CO}_2(g)$  can adsorb to, and react with, the surface, to form small quantities of carbonate. The refinement results are given in Table S-1 (Supporting Information), and the representative fit is shown in Figure 7b. It was not possible to refine relative occupancies on the Ti and Fe sites into stable values. This was anticipated because Ti and Fe have the similar X-ray scattering power. However, another way of telling if the Fe is doping into the material is to monitor the lattice parameters. In Figure 7 we plot the iron concentration dependence of the unit cell volume for the low-doped  $\text{BaFe}_x\text{Ti}_{1-x}\text{O}_3$  series of samples fit with the NT-BFTO+BCO model as shown in Table S-1 (Supporting Information). We find that the unit cell volume increases monotonically with increasing Fe content, providing additional evidence that Fe is being incorporated into the lattice of the perovskite BTO structure, consistent with the observations of the powder XRD (Figure 2) and XPS data. The experimental results independently offer verification of the same trend that an increase in lattice parameters occurs on incorporation of the iron into the perovskite. Since  $\text{Fe}^{4+}$  is a smaller ion than the  $\text{Ti}^{4+}$  that it is replacing, it therefore makes sense to assume that some of the iron is being incorporated as 3+ in the HS state, alongside  $\text{Fe}^{4+}$ . To maintain charge balance, this would imply that a significant number of oxygen vacancies ( $V_{\text{O}}^{2+}$ ) would have to also be arriving into the structure.<sup>68,69</sup> Such vacancies may be more easily accommodated due to the large surface to volume ratio for these sub-10 nm uniform nanocrystals. The XPS data confirms increasing  $\text{Fe}^{3+}(\text{HS})$ . Following the guidelines provided by Table 1, it is concluded that the nanocrystals have

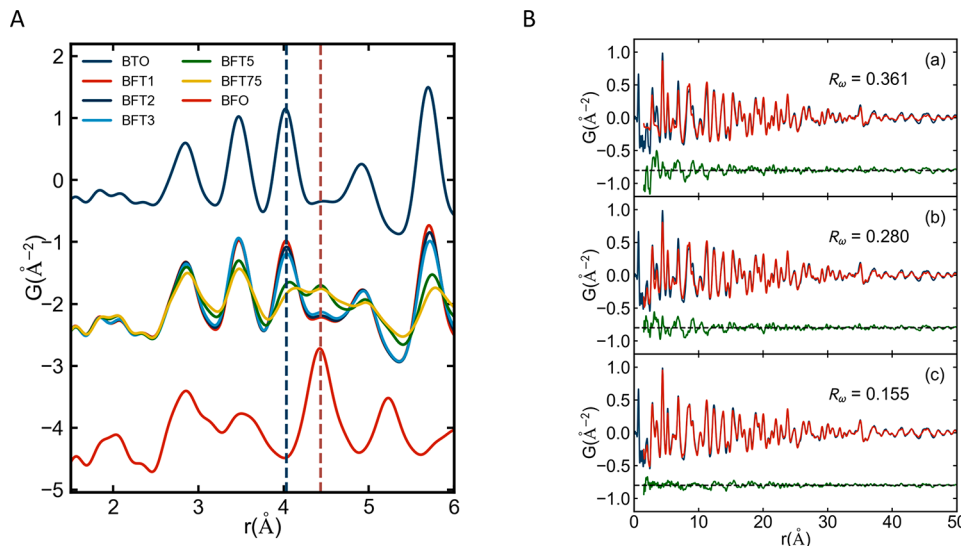


**Figure 8.** A: Experimental PDFs of all iron doped BFT samples for comparison. Top curve: pure BTO sample,  $x = 0$  (blue). Bottom curve: pure BFO sample,  $x = 1$  (brown). Curves in the middle: Ti–Fe mixed composition samples. The blue vertical dashed line highlights the strong  $r = 4.03 \text{ \AA}$  peak from the BTO data coming from Ba–Ba, Ti–Ti, and O–O bond lengths. The brown vertical dashed line highlights the strong  $r = 4.43 \text{ \AA}$  peak from the BFO data. B: X-ray PDFs of the the BFO ( $x = 1.0$ ) data (blue curves) with the best-fit calculated PDFs (red) for the (a) BCO, (b) BCO + BFO<sub>3</sub> and (c) BCO + BF<sub>2</sub>O<sub>4</sub> models. The difference curves are shown in green.

the potential to be multiferroic, given evidence of retention of tetragonality, lattice expansion to accommodate Fe<sup>3+</sup>(HS), XPS evidence of Fe<sup>3+</sup> as well as Fe<sup>4+</sup>, and the magnetic characterization discussed in Part IV.

The lattice parameters could go up or down with Fe doping depending on the valence and spin state of the iron. This is true whether referring to Shannon ionic radii or Pauling ionic radii.<sup>70</sup> In general, for 6-coordinate octahedral crystal environments, Ti(IV) is marginally larger than Fe(III)LS (8% larger) or Fe(IV) (3% larger) but smaller than Fe(II)HS or Fe(III)HS (19% and 5% smaller respectively). Therefore, an increase in unit-cell volume with  $x$ , such as a 1.3% increase in volume for 30% Fe incorporation, is an indication of Fe(III)HS incorporation, as well as Fe(IV). From Table S-1 (Supporting Information) we see that the Ti/Fe site refines to a value away from the high symmetry position in all these compounds. We note that the tetragonality,  $c/a$ , also increases with  $x$ , as shown in Figure 7. This could be an indication of changing multiferroicity, namely, that ferroelectricity (due to increased distortion of the central B atom from a centrosymmetric site) is strengthening with increasing Fe content. The ADPs of the Ti/Fe and Ba ions also increase slightly with higher  $x$ , consistent with some structural disorder from chemical substitution effects when Fe is doped into the lattice.

$\text{BaTi}_{1-x}\text{Fe}_x\text{O}_3$  ( $x > 3$ ). For higher doped samples there are significant changes in the PDF, as shown in Figure 8. It was concluded that the nanocrystals themselves became a partially mixed set of phases, despite being a dispersible nanoparticulate format. Comparing peaks in the BFO end member sample with the new peaks emerging in the high-doped BFTO samples suggests the new phase appearing leads to an end result of BFO, in which BFO is a combination of  $\text{BaFe}_x\text{Ti}_{1-x}\text{O}_3$  and phases for which Fe content is richer. There is a peak in the BTO data at  $r = 4.03 \text{ \AA}$  that is absent in the BFO data and a strong peak at  $r = 4.43 \text{ \AA}$  in the BFO end member that is not in BTO. The high doped BFT5 and BFT75 ( $x = 0.5$  and 0.75) PDFs clearly contain both characteristic peaks, suggesting that these samples are mixed phase. These peaks are highlighted in Figure 8 with

vertical dashed lines. As a result, solving the structure for the BFO sample first is the key to solving the mixed phase samples. Initially, it was not possible to fit the BFO data well with any reported model for BaFeO<sub>3</sub>, for a variety of published space groups, including  $Pm\bar{3}m$ ,<sup>64</sup>  $P4/mmm$ ,<sup>71</sup>  $R\bar{3}m$ ,<sup>72</sup>  $R3c$ ,<sup>71</sup>  $R3m$ ,<sup>72</sup> and  $P63mmc$ .<sup>73</sup> A slightly yet not completely satisfactory fit was found by including a refinement of BCO contamination (Figure 8a), attributed to reactive adsorption of CO<sub>2</sub> on the highly basic BaO surface layers of the BTO nanocrystals.<sup>62</sup> Due to the observation of extra signal in the difference curve in the low- $r$  region, we postulated the emergence of barium ferrite (BaFe<sub>2</sub>O<sub>4</sub>) as a model to consider. The results in this instance are inconclusive yet offer a worthy consideration: the BaFeO<sub>3</sub> perovskite model works reasonably well (Figure 8b), but a much better fit can be obtained using a model for orthorhombic BaFe<sub>2</sub>O<sub>4</sub> (BF<sub>2</sub>O<sub>4</sub> model), where a two-phase fit resulted in a  $R_w$  of 0.155 (Figure 8c). XPS data suggested the presence of Fe<sup>4+</sup> for  $x > 0.5$ , therefore favoring the model of BaFeO<sub>3</sub>, in which the B site oxidation state is formally IV, compared to BaFe<sub>2</sub>O<sub>4</sub> for which Fe is (III). In addition the model refined lattice parameters are noticeably different from one previously reported value for crystalline BaFe<sub>2</sub>O<sub>4</sub>:  $a = 18.995 \text{ \AA}$ ,  $b = 6.973 \text{ \AA}$ , and  $c = 11.300 \text{ \AA}$ , compared to  $a = 17.347 \text{ \AA}$ ,  $b = 9.336 \text{ \AA}$ , and  $c = 10.882 \text{ \AA}$ .<sup>65</sup> Further discussion is provided in the Supporting Information.

We conclude that, in the nanoscale  $\text{BaFe}_x\text{Ti}_{1-x}\text{O}_3$  system for values of  $x \leq 3$ , synthetic substitution occurs seamlessly and a single-phase compound is maintained, with substitution at the B site of Ti for Fe, as a mixture of Fe<sup>3+</sup>/Fe<sup>4+</sup>. Although not precisely quantified, it is postulated therefore that the structure may contain oxygen vacancies (especially at the surface) with increasing  $x$ , of the form  $\text{BaTi}_{1-x}\text{Fe}_x\text{O}_{3-\delta}$ . With increasing Fe concentration (especially  $x > 5$ ), the morphology of the nanocrystals is still largely intact, and the material can be dispersed in organic solvents, converted into films, etc., but the perovskite structure appears to have become less stable, devolving into additional competing phases. Some BaCO<sub>3</sub> is

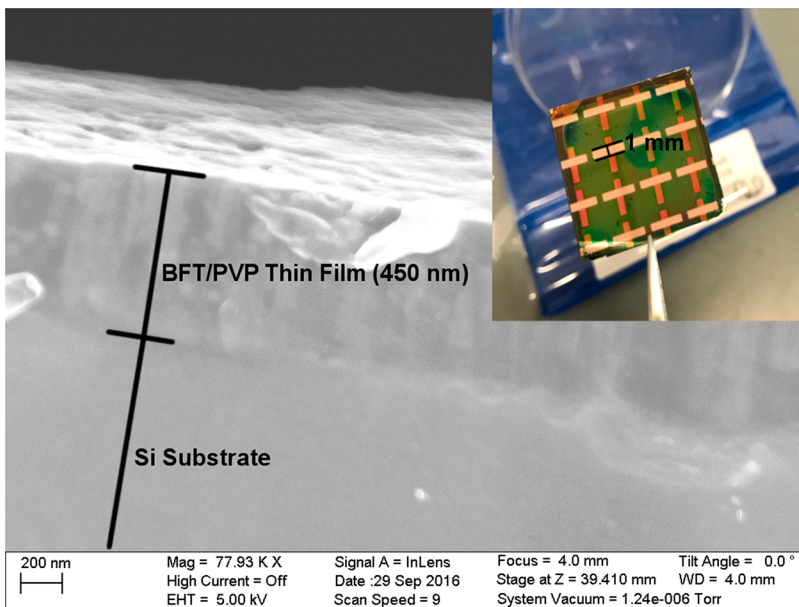


**Figure 9.** Cross sectional SEM micrograph of a typical BFT/PVP thin film nanocomposite. The average thickness of these nanocomposites was 450 nm. (Inset) Image of the capacitors showing the size of the electrodes.

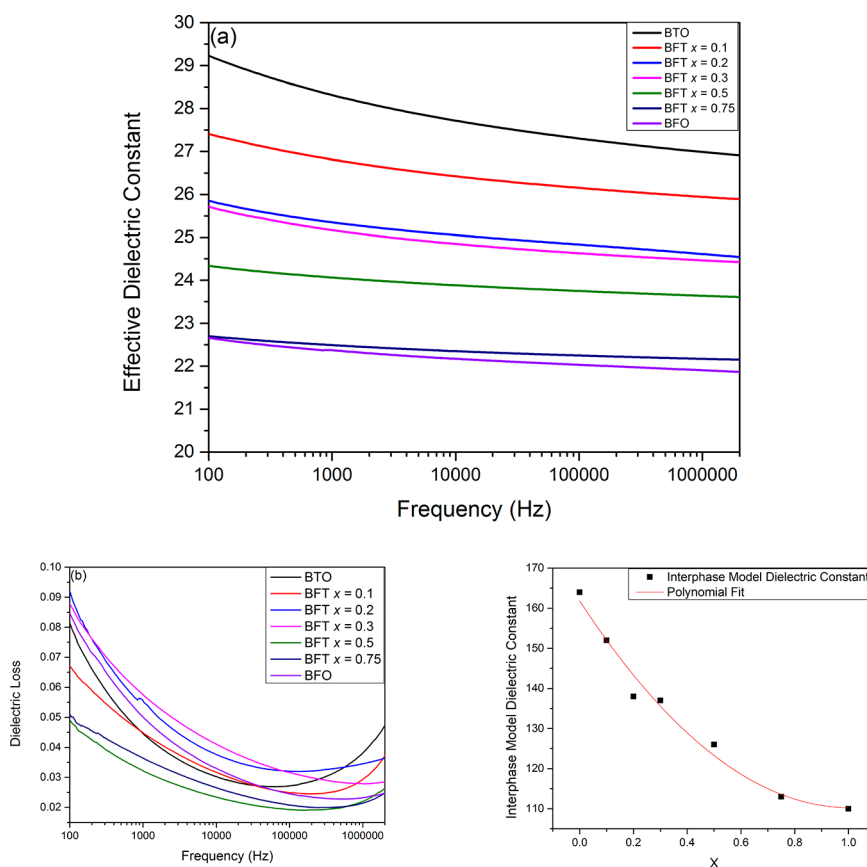


**Figure 10.** (a) Effective dielectric constant as a function of frequency for BTO, BFT,  $x = 0.1\text{--}0.3, 0.5$ , and  $0.75$ , and BFO. (b) Dielectric loss as a function of frequency for BTO, BFT,  $x = 0.1\text{--}0.3, 0.5$ , and  $0.75$ , and BFO. Dielectric constant decreases with increasing Fe concentration. (c) Plot of estimated intrinsic dielectric constants of the BFT nanocrystals as a function of  $x$ , calculated by applying the interphase model, with known volume fractions and electrode area.

present, and while  $\text{BaFe}_x\text{Ti}_{1-x}\text{O}_3$  is evident for  $x > 5$ , some  $\text{BaFe}_3\text{O}_3$  or  $\text{BaFe}_2\text{O}_4$  (or possibly both) may be forming.

### Part III: Device Fabrication, Dielectric, and Magnetic Characterization of the $(\text{BaTi}_{1-x}\text{Fe}_x\text{O}_3)$ System

Polymer–nanoparticle 0-3 nanocomposites over the range of compositions were prepared in order to study the dielectric properties as thin films. Due to how the dielectric constant is obtained for such a sample, great care is required when making a frequency

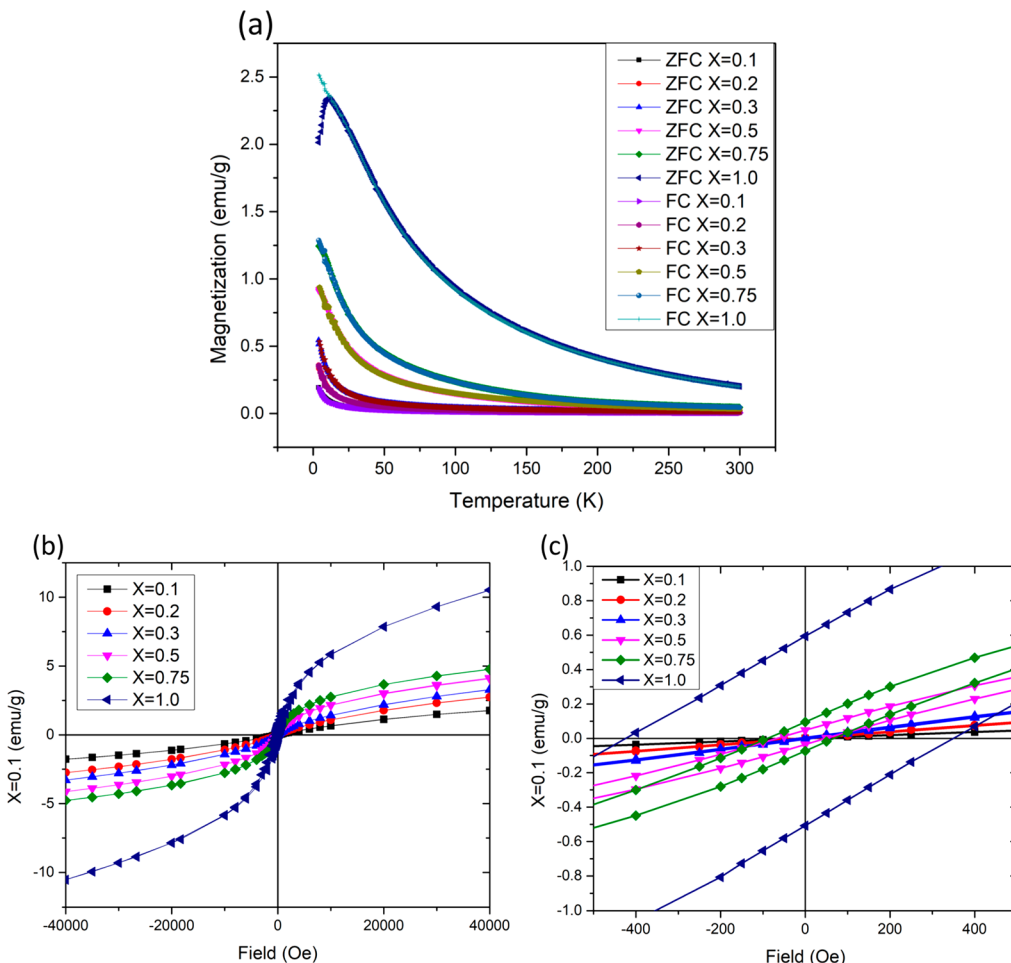


**Figure 11.** (a) ZFC and FC measurements of BFT  $x = 0.1\text{--}0.3, 0.5, 0.75$ , and  $1.0$  samples, (b) magnetic hysteresis measurements of BFT,  $x = 0.1\text{--}0.3$ ,  $0.5$ , and  $0.75$  samples, and (c) zoomed in portion of Figure 11b to highlight asymmetric hysteresis loops at higher Fe concentration.

dependent measurement. In chemical solution deposition of nanocrystals, a thin film (comprised of solely nanoparticles) will have a large percentage of void space no matter how compact the particles may be. These interstitial void spaces coupled with the electrode–dielectric interface can contribute to charge effects. In these cases Maxwell–Wagner–Sillars polarization effect is frequently observed (space charge), along with the contributions of adsorbed mobile species such as  $\text{H}_2\text{O}$  and  $\text{CO}_2$ . In order to minimize this effect and enable stable dielectric measurements, a layer of polyvinylpyrrolidone (PVP), suspended in ethanol, was spin coated in order to backfill the void space and act as an insulating layer.

In the samples prepared, silver electrodes were thermally evaporated onto a silicon substrate and a suspension of  $20\text{ mg/mL}$  BTO, BFT, or BFO was spin coated onto the surface of the electrode. In order to prevent this, polyvinylpyrrolidone (PVP), suspended in ethanol, was spin coated in order to backfill the void spaces and also acted as an insulating layer to prevent absorption of  $\text{H}_2\text{O}$  on the surface of the nanoparticles. The thin film nanocomposites were typically  $450\text{ nm}$  thick as seen in the cross sectional SEM micrograph in Figure 9. The samples were all heated to  $90\text{ }^\circ\text{C}$  for  $6\text{ h}$  before making impedance measurements to ensure all of the solvents had evaporated. The cross section of the electrodes was  $1\text{ mm}^2$ , which allowed for consistent calculation of the effective dielectric constant of the  $0\text{--}3$

nanocomposite consisting of nanoparticle filler and dielectric polymer host.

Effective permittivity of the BT/PVP, BFT/PVP, and BFO/PVP nanocomposites were measured over the frequency range of  $100\text{ Hz}$  to  $2\text{ MHz}$ . Multiple capacitors (12–16) were prepared for each film by metal evaporation of  $1\text{ mm}^2$  electrodes. The dielectric loss was also measured on the same instrument. In Figure 9, it is also shown that the dielectric polymer, PVP, has likely successfully infiltrated the thin film of BFT and filled the void spaces between nanoparticles. This is further confirmed in the stability of the measurements of the effective dielectric constant over a standard range of frequencies ( $100\text{ Hz}\text{--}2\text{ MHz}$ , relatively flat lines) in Figure 10. This observation is strong evidence that the measurement of the effective dielectric constant acquired using impedance analysis is due to the intrinsic nature of the material and not from interstitial charging or space charging due to void spaces within the  $0\text{--}3$  nanocomposite. The dielectric loss ( $\tan \delta$ ) values were in the range of  $0.02\text{--}0.09$  with the dielectric loss rising in the higher frequency range as seen in Figure 10b. This slight increase in dielectric loss at higher frequencies ( $>10^5\text{ Hz}$ ) is due to contact resistance which is known to make a significant contribution to the dielectric loss at higher frequencies.<sup>74</sup> The dielectric loss values at  $1\text{ MHz}$  were, however, all  $\tan \delta < 0.04$ , demonstrating that the nanocomposite can function well as an insulating dielectric, a capacitor, or a potential multiferroic device.

**Table 4.** Tabulation of Curie–Weiss Fitting of the ZFC and FC Measurements as well as Values for Magnetic Saturation,  $M_s$  at 4 T, Remanent Magnetization,  $M_r$ , and Magnetic Coercivity,  $H_c$ , for BFT,  $x = 0.1\text{--}0.3, 0.5, 0.75$ , and 1.0, Samples

sample	Curie constant $C$	Weiss constant $\theta$	$M_s$ (4T)	$M_r$	$H_c$
BFT $x = 0.1$	1.32	-3.64	1.76	0.001	11
BFT $x = 0.2$	2.65	-3.71	2.74	0.003	15
BFT $x = 0.3$	4.38	-4.19	3.28	0.005	-15, 16
BFT $x = 0.5$	21.85	-17.77	4.13	0.047, -0.036	-66, 47
BFT $x = 0.75$	40.27	-24.09	4.77	0.095, -0.073	-90, 67
BFT $x = 1.0$				0.59, -0.50	351, -427.5

A trend of decreasing effective dielectric constant measurements with increasing Fe doping concentration is seen in Figure 10a. This is attributed to doping of  $\text{Fe}^{3+}$  on the  $\text{Ti}^{4+}$  B-site creating fewer polarizable dipoles within the crystal unit cell. The response of the electric dipoles of Fe cannot switch as quickly at higher frequencies in the same way as Ti electric dipoles. This trend in decreasing effective dielectric constant agrees well with Guo et al.<sup>40</sup>

It is possible to estimate the dielectric constants of the nanoparticles (BTO, BFT, and BFO) embedded in the polymer matrix (PVP) of the nanocomposites using the modified interphase model.<sup>75</sup> This model takes into account the particle shape/orientation as well as the interphase spacing between nanoparticles. The interphase can be composed of air, matrix, and filler, all of which can affect the interactions between nanoparticles embedded in a nanocomposite. Estimation of the intrinsic dielectric constant of the filler (in this case the nanocrystals) can be performed when the nanoparticle diameter is known and uniform, when the area of the electrodes, thickness of the film, and therefore size of the capacitor can be measured and when volume fraction of the filler can be estimated with high level of certainty.<sup>41,76</sup> When modeling a nanocomposite composed of nanoparticle fillers and polymer matrix host, the interphase region has air occlusions in it. Accordingly, the interphase dielectric constant can be attributed to polymer and air:

$$\epsilon_3^\beta = \epsilon_2^\beta + \varphi_a(1 - \epsilon_2^\beta)$$

where  $\epsilon_3$  is the dielectric constant of the interphase,  $\epsilon_2$  is the dielectric constant of the polymer host,  $\varphi_a$  is the volume fraction of air within the interphase, and  $\beta$  is a dimensionless parameter depending on the shape and orientation of the filler. The effective dielectric constant ( $\epsilon_{\text{eff}}$ ) of the 0-3 nanocomposite using the interphase dielectric can be written as

$$\epsilon_{\text{eff}}^\beta = \varphi_1 \epsilon_1^\beta + (1 - \varphi_1) \epsilon_2^\beta + \varphi'(1 - \epsilon_2^\beta)$$

where  $\varphi_1$  is the filler volume fraction,  $\epsilon_1$  is the filler dielectric constant, and  $\varphi'$  can be written as

$$\varphi' = \varphi_1 \frac{1 - \varphi_1}{1 + \varphi_1}$$

Using the modified interphase model, the dielectric constants of BTO, BFT,  $x = 0.1\text{--}0.3, 0.5, 0.75$ , and BFO were estimated to be 164, 152, 138, 137, 126, 113, and 110, respectively. It has been reported that the bulk dielectric constants of BTO, BFT, and BFO are significantly larger than our calculated values ( $>1000$ );<sup>3,77</sup> however, it is known that the size of the nanoparticles plays a significant role in the suppression of the ferroelectric behavior of the material, despite evidence of persistence of polarization. This is evident in the dielectric

measurements and consistent with other perovskite systems and nanocomposites.<sup>67</sup>

**Part IV: Magnetic Characterization of the  $(\text{BaTi}_{1-x}\text{Fe}_x\text{O}_3)$  Nanocrystal System.** The magnetic properties were analyzed in order to determine presence, extent, and type of magnetization. Previous reports have focused on larger particle sizes and/or different doping concentrations. In the case of nanocrystalline powders reported by Yang et al.,<sup>78</sup> Fe was successfully doped into  $\text{BaTiO}_3$  over a substantial composition range with particle size distributions in the 50–300 nm region, and M–H results indicated ferromagnetism with a weak coercive force and small remanent magnetization for the range  $x = 0.2\text{--}0.5$ , while paramagnetism was observed for  $x = 0.05, 0.1$ . In this case, the magnetic properties could be probed for discrete nanocrystals with  $<10$  nm dimensions. Characterization of the magnetic properties of BFT  $x = 0.1\text{--}0.3, 0.5, 0.75$ , and 1.0 was performed on a Quantum Designs Magnetic Property Measurement System (MPMS) at Oak Ridge National Laboratory in Tennessee. ZFC and FC measurements were taken on BFT  $x = 0.1\text{--}0.3, 0.5, 0.75$ , and 1.0 samples as seen in Figure 11a below. For ZFC measurements the samples were cooled to 5 K in the absence of an external magnetic field. Once at 5 K, an external magnetic field of 2000 Oe was applied to the samples, and they were slowly heated to 300 K. For the FC measurements, the samples were cooled down to 5 K in the presence of a 2000 Oe field. A sharp increase in magnetization is observed at 7, 15, 25, 50, 75, and 100 K for  $x = 0.1, 0.2, 0.3, 0.5, 0.75$ , and 1.0 samples, respectively. The highest values of magnetization observed in the FC measurement were 0.17 emu/g, 0.34 emu/g, 0.53 emu/g, 0.94 emu/g, 1.27 emu/g, and 2.5 emu/g for  $x = 0.1, 0.2, 0.3, 0.5, 0.75$ , and 1.0 samples, respectively, at 5 K. An increase in magnetization as a function of Fe content is observed and agrees well with literature.<sup>79,80</sup> A much larger increase in the magnetization is seen in the  $x = 1.0$  sample as there is no presence of  $\text{Ti}^{4+}$  in the crystal unit cell thus leading to a higher amount of magnetic spins aligning in the presence of a magnetic field, and as confirmed by PDF, the presence of a Ba–Fe–O material in minor quantity (determined to be  $\text{BaFeO}_3$ ) is also contributing. As the temperature is increased the magnetization decreases due to randomization of the magnetic orderings within the nanoparticles because of the thermal energy. This only becomes drastically apparent below 200 K. There is no observed splitting between the ZFC and FC measurements implying that the nanoparticles may be paramagnetic.

Magnetic hysteresis measurements were taken on BFT  $x = 0.1\text{--}0.3, 0.5, 0.75$ , and 1.0 at 5 K with a maximum sweeping magnetic field of 40 000 Oe as seen in Figure 11b below. A similar trend in increasing magnetization can be seen as a function of increasing Fe content in the nanocrystals. Upon closer inspection of the magnetic hysteresis loops in Figure 11c it is apparent that there is a weak magnetic coercivity and a small

remanence magnetization, implying a weak ferromagnetic state at low temperatures (<5 K); however, the samples never reach full magnetic saturation at this magnetic field strength.

For lower Fe concentrations ( $x \leq 0.2$ ) it is observed that the magnetic coercivity ( $H_c$ ) is 11 Oe for BFT  $x = 0.1$  and 15 Oe for BFT  $x = 0.2$  with relatively low remanent magnetization of 0.001 emu/g and 0.003 emu/g, respectively, as seen in Table 4 below. However, when Fe concentration is higher ( $x \geq 0.3$ ) there are different values for the negative and positive magnetic field values. This is seen in both the magnetic coercivity and the remanent magnetization. As the Fe concentration increases, the remanent magnetization and magnetic coercivity increase as well, and this is to be expected as more Fe–O octahedrons are forming, creating more magnetic moments due to doping concentration. The asymmetric hysteresis loops are thought to be due to the multiple valence states existing within the crystal lattice due to the presence of both  $\text{Fe}^{3+}$  and  $\text{Fe}^{4+}$  as seen in the XPS data in Figure 3d.<sup>69</sup> As Fe concentration increases, the different magnetic states become more and more apparent. The ZFC and FC data were fit to a Curie–Weiss law of which the Curie and Weiss constants were calculated (Table 4). A similar trend in the much larger increase in magnetization is seen in the hysteresis as well as the ZFC and FC curves and is likely due to the absence of  $\text{Ti}^{4+}$  in the unit cell as stated above.

## CONCLUSIONS

In conclusion, nanocrystals based on a  $(\text{BaTi}_{1-x}\text{Fe}_x\text{O}_3)$  system were prepared using a near room temperature ( $\leq 60^\circ\text{C}$ ) hybrid sol–gel chemical solution processing method. The samples were structurally characterized by XRD, TEM, XPS, and PDF. Initial powder XRD indicated highly crystalline samples with an increasing lattice parameter with increasing Fe inclusion. TEM/EDS and electron diffraction analysis showed discrete relatively monodisperse spherical single domain nanoparticles with an average size of 8 nm. EDS elemental mapping showed a uniform composition of Ba, Fe, Ti, and O. XPS analysis confirms the presence of both  $\text{Fe}^{3+}(d^5)$  and  $\text{Fe}^{4+}(d^4)$ , both candidates for multiferroicity in this system, given low spin configurations in octahedral field splitting. XPS also shows an increasing amount of  $\text{Fe}^{4+}$  with increasing Fe, suggesting that Fe(IV) is evolving in order to account for charge compensation with decreasing quantities of  $\text{Ti}^{4+}$ , while still attempting to preserve the perovskite structure. However, the increase in lattice parameters with the increase in the concentration of Fe (observed by powder XRD and PDF) corresponds to a doping of  $\text{Fe}^{3+}$  on the  $\text{Ti}^{4+}$  site within the crystal lattice. A mixture of  $\text{Fe}^{3+}/\text{Fe}^{4+}$  ends up residing at the B site:  $\text{Fe}^{4+}$  helps stabilize the structure through charge balancing, while  $\text{Fe}^{3+}$  may be complimented with oxygen vacancies to some extent, especially at the surface. The structure may therefore be of the form  $\text{BaTi}_{1-x}\text{Fe}_x\text{O}_{3-\delta}$  for increasing  $x$ . Eventually, with increasing Fe ( $x > 0.5$ ), neither  $\text{Fe}^{3+}$  nor  $\text{Fe}^{4+}$  can maintain the structure, and the emergence of more thermodynamically stable Ba–Fe–O phases start to emerge. PDF analysis fully supports the observation that Fe substitution is facile for  $x = 0.1, 0.2, 0.3$ , generating a series of compounds that appear mainly monophasic, but at higher Fe substitutions the  $\text{BaTi}_{1-x}\text{Fe}_x\text{O}_3$  nanocrystals show evidence of other (trace) phases being present but still present similar structural characteristics, suggesting that Fe substitution is also possible at  $\text{Fe} > 0.5$ . Pair distribution function (PDF) analysis enabled in-depth structural characterization (phase, space group, unit cell parameters, etc.). PDF shows that, in the case of  $x = 0, 0.1, 0.2, 0.3$ ,  $\text{BaTiO}_3$  and  $\text{BaTi}_{1-x}\text{Fe}_x\text{O}_3$  nanocrystals are concluded to be

tetragonal noncentrosymmetric  $P4mm$  with lattice parameters increasing from, e.g.,  $c = 4.04$  to  $4.08\text{ \AA}$ . Due to the larger cationic radii of  $\text{Fe}^{3+}$  ions when compared to  $\text{Ti}^{4+}$ , an increase in lattice parameter,  $a$ , is anticipated. The observation of noncentrosymmetry confers that spontaneous polarization (and therefore possible ferroelectric behavior), due to displacement of the B site cation, is possible at this 8–10 nm length scale, consistent with other recent reports. For  $x > 0.5$ , Fe evidently impacts the structure but still produces dispersible, relatively monodisperse nanocrystals, with additional phases growing in. The decreased precursor reactivity of  $\text{Fe}(\text{OCH}(\text{CH}_3)_3)$ , when compared to  $\text{Ti}(\text{OCH}(\text{CH}_3)_3)$  is a factor. For  $x = 1.0$ , both  $\text{BaFeO}_3$  and  $\text{BaFe}_2\text{O}_4$  were modeled and  $\text{BaFeO}_3$  considered to be the more likely fit by PDF, supported also by XPS. XPS analysis showed the presence of  $\text{Fe}^{4+}$  ions suggesting a mixed valence of Fe within the crystal structure at higher concentrations of Fe ( $x \geq 0.3$ ) which agreed well with the asymmetric magnetic hysteresis loops observed for the three samples  $x = 0.3, 0.5, 0.75$ , and 1.0.

Magnetic characterization by MPMS (both magnetic hysteresis loops and zero field and field cooling measurements) showed increased magnetization with increasing Fe ion concentration. Weak magnetic coercivity and a small remanent magnetization is observed (<5 K), implying a weak ferromagnetic state at low temperatures (<5 K). A suspended solution of the nanoparticles in ethanol was spin coated onto thermally evaporated silver electrodes along with PVP in order to make 0–3 nanocomposite capacitors for dielectric measurements. Because of the good dispersibility of the nanocrystals in solvents, spin coating of uniform 0–3 nanocomposite  $\text{BaTi}_{1-x}\text{Fe}_x\text{O}_3/\text{polyvinylpyrrolidone}$  thin film capacitors ( $<0.5\text{ }\mu\text{m}$ ) was possible. Frequency dependent dielectric measurements showed stable dielectric constants at 1 MHz of 27.0 to 22.2 for  $\text{BaTi}_{1-x}\text{Fe}_x\text{O}_3$  samples for  $x = 0$ –0.75, respectively. Loss tangent values at 1 MHz were  $\sim 0.04$ , demonstrating the ability to prepare capacitors of magnetic  $\text{Ba}(\text{Ti}_{1-x}\text{Fe}_x)\text{O}_3$  with relatively high permittivity, further indication of a reasonably high  $k$  intrinsic to the nanocrystals. The effective dielectric constants showed a trend in decreasing effective dielectric constant as a function of increasing Fe concentration in the sample, likely due to the  $\text{Fe}^{3+}$  ions providing fewer polarizable dipoles in the crystalline structure. The dielectric loss measurements showed a dielectric loss between 0.02 and 0.09 showing a well-insulated nanocomposite free of void spaces. The low loss magnetodielectric devices suggest future opportunities for exploration of multi-ferroic nanocomposites based on this material and such design processes.

## ASSOCIATED CONTENT

### S Supporting Information

The Supporting Information is available free of charge on the ACS Publications website at DOI: [10.1021/acs.chemmater.8b04447](https://doi.org/10.1021/acs.chemmater.8b04447).

Figure S1 shows an image used for EDS analysis shown in Figure 4d; further details are given for the PDF total scattering technique for determining local order in nanostructured materials; PDF analysis is explained in brief with references and key equations; and Table S1 shows structure refinement results of the NT-BFTO +BCO model fit to the low-doped  $\text{BaFe}_x\text{Ti}_{1-x}\text{O}_3$  ( $x = 0.1, 0.2, 0.3$ ) sample PDFs, i.e., BFT1 to BFT3, over a range of  $1.5 < r < 50\text{ \AA}$  ([PDF](#))

## AUTHOR INFORMATION

### Corresponding Author

\*(S. O'Brien) E-mail: [sobrien@ccny.cuny.edu](mailto:sobrien@ccny.cuny.edu).

### ORCID

Julien Lombardi: [0000-0003-1307-1089](https://orcid.org/0000-0003-1307-1089)

Long Yang: [0000-0001-8731-0172](https://orcid.org/0000-0001-8731-0172)

Frederick A. Pearsall: [0000-0003-1577-3746](https://orcid.org/0000-0003-1577-3746)

Nasim Farahmand: [0000-0001-7543-6886](https://orcid.org/0000-0001-7543-6886)

Zheng Gai: [0000-0002-6099-4559](https://orcid.org/0000-0002-6099-4559)

Simon J. L. Billinge: [0000-0002-9734-4998](https://orcid.org/0000-0002-9734-4998)

Stephen O'Brien: [0000-0001-7531-8900](https://orcid.org/0000-0001-7531-8900)

### Notes

The authors declare no competing financial interest.

## ACKNOWLEDGMENTS

This work was supported by the National Science Foundation, under NSF DMR Award No. 1461499, and with an additional support from NSF CREST No. 1547830. S.O. and F.A.P. are also grateful to AGEP award supplement NSF DMR No. 1831127, on behalf of F.A.P. S.O. and F.A.P. are grateful to Jackie Li for useful discussions. F.A.P. is grateful to Tai-De Li for help with the XPS. J.L. and F.A.P. are grateful to Jorge Morales for help with the EM. All magnetic characterization was conducted at the Center for Nanophase Materials Sciences (ORNL) which is a DOE Office of Science User Facility. X-ray PDF measurements were conducted on beamline 28-ID-2 of the National Synchrotron Light Source II, a U.S. Department of Energy (DOE) Office of Science User Facility operated for the DOE Office of Science by Brookhaven National Laboratory under Contract No. DE-SC0012704. L.Y. and S.J.L.B.'s effort on PDF analysis and modeling was supported by the NSF MRSEC program through Columbia in the Center for Precision Assembly of Superstratic and Superatomic Solids (DMR-1420634).

## REFERENCES

- (1) Wolf, S. A. Spintronics: A Spin-Based Electronics Vision for the Future. *Science* **2001**, *294*, 1488.
- (2) Spaldin, N. A.; Cheong, S. W.; Ramesh, R. Multiferroics: Past, Present, and Future. *Phys. Today* **2010**, *63*, 38–43.
- (3) Rani, A.; Kolte, J.; Vadla, S. S.; Gopalan, P. Structural, Electrical, Magnetic and Magnetoelectric Properties of Fe Doped BaTiO<sub>3</sub> Ceramics. *Ceram. Int.* **2016**, *42*, 8010–8016.
- (4) Bibes, M.; Barthélémy, A. Towards a Magnetoelectric Memory. *Nat. Mater.* **2008**, *7*, 425–426.
- (5) Scott, J. F. Room-Temperature Multiferroic Magnetoelectrics. *NPG Asia Mater.* **2013**, *5*, No. e72.
- (6) Fiebig, M.; Lottermoser, T.; Meier, D.; Trassin, M. The Evolution of Multiferroics. *Nat. Rev. Mater.* **2016**, *1*, 16046.
- (7) Nikonorov, D. E.; Young, I. A. Overview of Beyond-CMOS Devices and a Uniform Methodology for Their Benchmarking. *Proc. IEEE* **2013**, *101*, 2498–2533.
- (8) Manipatruni, S.; Nikonorov, D. E.; Young, I. A. Beyond CMOS Computing with Spin and Polarization. *Nat. Phys.* **2018**, *14*, 338–343.
- (9) Dowben, P. A.; Binek, C.; Zhang, K.; Wang, L.; Mei, W.-N.; Bird, J. P.; Singisetti, U.; Hong, X.; Wang, K. L.; Nikonorov, D. Towards a Strong Spin-Orbit Coupling Magneto-Electric Transistor. *IEEE J. Explor. Solid-State Comput. Devices Circuits* **2018**, *4*, 1–9.
- (10) Zhu, M.; Nan, T.; Liu, M.; Ren, W.; Zhou, Z.; Sun, N. X. Voltage Tuning of Ferromagnetic Resonance and Linewidth in Spinel Ferrite/Ferroelectric Multiferroic Heterostructures. *IEEE Magn. Lett.* **2015**, *6*, 1–4.
- (11) Spaldin, N. A. The Renaissance of Magnetoelectric Multiferroics. *Science* **2005**, *309*, 391.
- (12) Spaldin, N. A. Multiferroics: Past, Present, and Future. *MRS Bull.* **2017**, *42*, 385–389.
- (13) Ortega, N.; Kumar, A.; Katiyar, R. S.; Rinaldi, C. Dynamic Magneto-Electric Multiferroics PZT/CFO Multilayered Nanostructure. *J. Mater. Sci.* **2009**, *44*, 5127–5142.
- (14) Gupta, R.; Shah, J.; Chaudhary, S.; Singh, S.; Kotnala, R. K. Magnetoelectric Coupling-Induced Anisotropy in Multiferroic Nano-composite (1 - X)BiFeO<sub>3</sub>-xBaTiO<sub>3</sub>. *J. Nanopart. Res.* **2013**, DOI: [10.1007/s11051-013-2004-8](https://doi.org/10.1007/s11051-013-2004-8).
- (15) Wang, J.; Neaton, J. B.; Zheng, H.; Nagarajan, V.; Ogale, S. B.; Liu, B.; Viehland, D.; Vaithyanathan, V.; Schlom, D. G.; Waghmare, U. V.; et al. Epitaxial BiFeO<sub>3</sub> Multiferroic Thin Film Heterostructures. *Science* **2003**, *299*, 1719–1722.
- (16) Fiebig, M.; Lottermoser, T.; Meier, D.; Trassin, M. The Evolution of Multiferroics. *Nat. Rev. Mater.* **2016**, *1*, 16046.
- (17) Keeble, D. S.; Thomas, P. A. On the Tetragonality of the Room-Temperature Ferroelectric Phase of Barium Titanate, BaTiO<sub>3</sub>. *J. Appl. Crystallogr.* **2009**, *42*, 480–484.
- (18) Spanier, J. E.; Kolpak, A. M.; Urban, J. J.; Grinberg, I.; Ouyang, L.; Yun, W. S.; Rappe, A. M.; Park, H. Ferroelectric Phase Transition in Individual Single-Crystalline BaTiO<sub>3</sub> Nanowires. *Nano Lett.* **2006**, *6*, 735–739.
- (19) Smith, M. B.; Page, K.; Siegrist, T.; Redmond, P. L.; Walter, E. C.; Seshadri, R.; Brus, L. E.; Steigerwald, M. L. Crystal Structure and the Paraelectric-to-Ferroelectric Phase Transition of Nanoscale BaTiO<sub>3</sub>. *J. Am. Chem. Soc.* **2008**, *130*, 6955–6963.
- (20) Page, K.; Proffen, T.; Niederberger, M.; Seshadri, R. Probing Local Dipoles and Ligand Structure in BaTiO<sub>3</sub> Nanoparticles. *Chem. Mater.* **2010**, *22*, 4386–4391.
- (21) Polking, M. J.; Han, M. G.; Yourdkhani, A.; Petkov, V.; Kisielowski, C. F.; Volkov, V. V.; Zhu, Y.; Caruntu, G.; Paul Alivisatos, A.; Ramesh, R. Ferroelectric Order in Individual Nanometre-Scale Crystals. *Nat. Mater.* **2012**, *11*, 700–709.
- (22) Shi, C.; Billinge, S. J. L.; Puma, E.; Bang, S. H.; Bean, N. J. H.; De Sugny, J. C.; Gambee, R. G.; Haskell, R. C.; Hightower, A.; Monson, T. C. Barium Titanate Nanoparticles: Short-Range Lattice Distortions with Long-Range Cubic Order. *Phys. Rev. B: Condens. Matter Mater. Phys.* **2018**, *98*, 085421.
- (23) Buscaglia, M. T.; Bassoli, M.; Buscaglia, V.; Vormberg, R. Solid-State Synthesis of Nanocrystalline BaTiO<sub>3</sub>: Reaction Kinetics and Powder Properties. *J. Am. Ceram. Soc.* **2008**, *91*, 2862–2869.
- (24) Lemoine, C.; Gilbert, B.; Michaux, B.; Pirard, J. P.; Lecloux, A. Synthesis of Barium Titanate by the Sol-Gel Process. *J. Non-Cryst. Solids* **1994**, *175*, 1–13.
- (25) Chen, H.-J.; Chen, Y.-W. Hydrothermal Synthesis of Barium Titanate. *Ind. Eng. Chem. Res.* **2003**, *42*, 473–483.
- (26) Ramesh, S.; Shutzberg, B. A.; Huang, C.; Giannelis, E. P.; Gao, J. Dielectric Nanocomposites for Integral Thin Film Capacitors: Materials Design, Fabrication and Integration Issues. *IEEE Trans. Adv. Packag.* **2003**, *26*, 17–24.
- (27) Fortunato, E.; Barquinha, P.; Martins, R. Oxide Semiconductor Thin-Film Transistors: A Review of Recent Advances. *Adv. Mater.* **2012**, *24*, 2945–2986.
- (28) Das, R. N.; Markovich, V. R. Nanomaterials for Electronic Packaging: Toward Extreme Miniaturization. *IEEE Nanotechnol. Mag.* **2010**, *4*, 18–26.
- (29) Ren, X. Large Electric-Field-Induced Strain in Ferroelectric Crystals by Point-Defect-Mediated Reversible Domain Switching. *Nat. Mater.* **2004**, *3*, 91–94.
- (30) Costanzo, T.; McCracken, J.; Rotaru, A.; Caruntu, G. Quasi-Monodisperse Transition-Metal-Doped BaTiO<sub>3</sub> (M = Cr, Mn, Fe, Co) Colloidal Nanocrystals with Multiferroic Properties. *ACS Appl. Nano Mater.* **2018**, *1*, 4863–4874.
- (31) Liu, S.; Huang, L.; Li, W.; Liu, X.; Jing, S.; Li, J.; O'Brien, S. Green and Scalable Production of Colloidal Perovskite Nanocrystals and Transparent Sols by a Controlled Self-Collection Process. *Nanoscale* **2015**, *7*, 11766–11776.
- (32) Van Tassell, B.; Yang, S.; Le, C.; Huang, L.; Liu, S.; Chando, P.; Liu, X.; Byro, A.; Gerber, D. L.; Leland, E. S.; et al. Metacapacitors:

- Printed Thin Film, Flexible Capacitors for Power Conversion Applications. *IEEE Trans. Power Electron.* **2016**, *31*, 2695–2708.
- (33) Uchino, K. *Ferroelectric Devices*, 2nd ed.; CRC Press: New York, 2009.
- (34) Rabe, K. M.; Dawber, M.; Lichtensteiger, C.; Ahn, C. H.; Triscone, J.-M. Modern Physics of Ferroelectrics: Essential Background. *Physics (College Park Md.)*. **2007**, *105*, 1–30.
- (35) Gaudon, M. Out-of-Centre Distortions around an Octahedrally Coordinated  $Ti^{4+}$  in  $BaTiO_3$ . *Polyhedron* **2015**, *88*, 6–10.
- (36) Bersuker, I. B. Pseudo Jahn-Teller Origin of Perovskite Multiferroics, Magnetic- Ferroelectric Crossover, and Magnetoelectric Effects: The  $d^0-d^{10}$  Problem. *Phys. Rev. Lett.* **2012**, *108*, 137202.
- (37) Bersuker, I. B. Pseudo-Jahn-Teller Effect - A Two-State Paradigm in Formation, Deformation, and Transformation of Molecular Systems and Solids. *Chem. Rev.* **2013**, *113*, 1351–1390.
- (38) Hill, N. A. Why Are There so Few Magnetic Ferroelectrics? *J. Phys. Chem. B* **2000**, *104*, 6694–6709.
- (39) Mukhopadhyay, S.; Chen, T. Surface Chemical States of Barium Titanate: Influence of Sample Processing. *J. Mater. Res.* **1995**, *10*, 1502.
- (40) Guo, Z.; Yang, L.; Qiu, H.; Zhan, X.; Yin, J.; Cao, L. Structural, Magnetic and Dielectric Properties of Fe-Doped  $BaTiO_3$  Solids. *Mod. Phys. Lett. B* **2012**, *26*, 1250056.
- (41) Pearsall, F. A.; Lombardi, J.; O'Brien, S. Monomer Derived Poly(Furfuryl)/ $BaTiO_3$  0–3 Nanocomposite Capacitors: Maximization of the Effective Permittivity Through Control at the Interface. *ACS Appl. Mater. Interfaces* **2017**, *9*, 40324–40332.
- (42) Ayouchi, R.; Marton, F.; Leinen, D.; Ramos-Barrado, J. R. Compositional, Structural and Electrical Characterization of Barium Titanate Thin Films Prepared on Fused Silica and Si (111) by Spray Pyrolysis. *Surf. Interface Anal.* **2000**, *30*, 565–569.
- (43) Fujii, T.; Voogt, F. C.; Hibma, T.; Sawatzky, G. A. In Situ XPS Spectra of Nonstoichiometric  $Fe_{3-\delta}O_4$  (100) Films. *Surf. Sci. Spectra* **1999**, *6*, 337–346.
- (44) Kubelka, P.; Munk, F. Ein Beitrag Zur Optik Der Farbanstriche. *Z. Techn. Phys.* **1931**, *12*, 593–601.
- (45) Hecht, H. G. The Interpretation of Diffuse Reflectance Spectra. *J. Res. Natl. Bur. Stand., Sect. A* **1976**, *80*, 567–583.
- (46) Tauc, J. Optical Properties and Electronic Structure of Amorphous Ge and Si. *Mater. Res. Bull.* **1968**, *3*, 37–46.
- (47) Fan, J.; Yu, C.; Wang, L.; Tu, B.; Zhao, D.; Sakamoto, Y.; Terasaki, O. Mesotunnels on the Silica Wall of Ordered SBA-15 to Generate Three-Dimensional Large-Pore Mesoporous Networks. *J. Am. Chem. Soc.* **2001**, *123*, 12113–12114.
- (48) Venkata Ramana, E.; Figueiras, F.; Mahajan, A.; Tobaldi, D. M.; Costa, B. F. O.; Graça, M. P. F.; Valente, M. A. Effect of Fe-Doping on the Structure and Magnetoelectric Properties of  $(Ba_{0.85}Ca_{0.15})-(Ti_{0.9}Zr_{0.1})O_3$  Synthesized by a Chemical Route. *J. Mater. Chem. C* **2016**, *4*, 1066–1079.
- (49) Egam, T.; Billinge, S. J. L. *Underneath the Bragg Peaks: Structural Analysis of Complex Materials*, 2nd ed.; Elsevier: Amsterdam, 2012.
- (50) Billinge, S. J. L.; Levin, I. The Problem with Determining Atomic Structure at the Nanoscale. *Science* **2007**, *316*, 561–565.
- (51) Chupas, P. J.; Qiu, X.; Hanson, J. C.; Lee, P. L.; Grey, C. P.; Billinge, S. J. L. Rapid-Acquisition Pair Distribution Function (RA-PDF) Analysis. *J. Appl. Crystallogr.* **2003**, *36*, 1342–1347.
- (52) Juhás, P.; Davis, T.; Farrow, C. L. L.; Billinge, S. J. L. PDFgetX3: A Rapid and Highly Automatable Program for Processing Powder Diffraction Data into Total Scattering Pair Distribution Functions. *J. Appl. Crystallogr.* **2013**, *46*, 560–566.
- (53) Farrow, C. L.; Juhás, P.; Liu, J. W.; Bryndin, D.; Božin, E. S.; Bloch, J.; Proffen, T.; Billinge, S. J. L. PDFfit2 and PDFgui: Computer Programs for Studying Nanostructure in Crystals. *J. Phys.: Condens. Matter* **2007**, *19*, 335219.
- (54) Juhás, P.; Farrow, C. L.; Yang, X.; Knox, K. R.; Billinge, S. J. L. Complex Modeling: A Strategy and Software Program for Combining Multiple Information Sources to Solve Ill Posed Structure and Nanostructure Inverse Problems. *Acta Crystallogr., Sect. A: Found. Adv.* **2015**, *71*, 562–568.
- (55) Farrow, C. L.; Ruan, C.; Billinge, S. J. L. Quantitative Nanoparticle Structures from Ultrafast Electron Crystallography Data, arXiv:0910.5232v1 [cond-mat.mtrl-sci], 2009.
- (56) Farrow, C. L.; Billinge, S. J. L. Relationship between the Atomic Pair Distribution Function and Small-Angle Scattering: Implications for Modeling of Nanoparticles. *Acta Crystallogr., Sect. A: Found. Crystallogr.* **2009**, *65*, 232–239.
- (57) Billinge, S. J. L.; Kanatzidis, M. G. Beyond Crystallography- the Study of Disorder, Nanocrystallinity and Crystallographically Challenged Materials with Pair Distribution Functions. *Chem. Commun.* **2004**, 749–760.
- (58) Shatnawi, M. T. Local Structure of GeSe Glasses around the Rigidity Percolation Threshold Using Atomic Pair Distribution Function and X-Ray Absorption Fine Structure Techniques. PhD Thesis, Michigan State University, 2007.
- (59) Yang, X.; Juhas, P.; Farrow, C. L.; Billinge, S. J. L. XPDSuite: An End-to-End Software Solution for High Throughput Pair Distribution Function Transformation, Visualization and Analysis. arXiv:1402.3163, 2015.
- (60) Jeong, I.-K.; Proffen, T.; Mohiuddin-Jacobs, F.; Billinge, S. J. L. Measuring Correlated Atomic Motion Using X-Ray Diffraction. *J. Phys. Chem. A* **1999**, *103*, 921–924.
- (61) Frazer, B. C.; Danner, H. R.; Pepinsky, R. Single-Crystal Neutron Analysis of Tetragonal  $BaTiO_3$ . *Phys. Rev.* **1955**, *100*, 745–746.
- (62) Rabuffetti, F. A.; Brutcher, R. L. Structural Evolution of  $BaTiO_3$  Nanocrystals Synthesized at Room Temperature. *J. Am. Chem. Soc.* **2012**, *134*, 9475–9487.
- (63) Antao, S. M.; Hassan, I. The Orthorhombic Structure of  $CaCO_3$ ,  $SrCO_3$ ,  $PbCO_3$  and  $BaCO_3$ : Linear Structural Trends. *Can. Mineral.* **2009**, *47*, 1245.
- (64) Hayashi, N.; Yamamoto, T.; Kageyama, H.; Nishi, M.; Watanabe, Y.; Kawakami, T.; Matsushita, Y.; Fujimori, A.; Takano, M.  $BaFeO_3$ : A Ferromagnetic Iron Oxide. *Angew. Chem., Int. Ed.* **2011**, *50*, 12547–12550.
- (65) Leib, W.; Müller-Buschbaum, Hk. Zur Verbindungsbildung  $MO:M_2O_3$  Eine Neue Form von  $BaFe_2O_4$  Mit Aufgefüllter Tridymitsruktur. *Z. Anorg. Allg. Chem.* **1986**, *538*, 71–77.
- (66) Hoshina, T. Size Effect of Barium Titanate: Fine Particles and Ceramics. *J. Ceram. Soc. Jpn.* **2013**, *121*, 156–161.
- (67) Huang, L.; Chen, Z.; Wilson, J. D.; Banerjee, S.; Robinson, R. D.; Herman, I. P.; Laibowitz, R.; O'Brien, S. Barium Titanate Nanocrystals and Nanocrystal Thin Films: Synthesis, Ferroelectricity, and Dielectric Properties. *J. Appl. Phys.* **2006**, *100*, 034316.
- (68) Zhao, T.; Chen, F.; Lu, H.; Yang, G.; Chen, Z. Thickness and Oxygen Pressure Dependent Structural Characteristics of Films Grown by Laser Molecular Beam Epitaxy Thickness and Oxygen Pressure Dependent Structural Characteristics of  $BaTiO_3$  Thin Films Grown by Laser Molecular Beam Epitaxy. *J. Appl. Phys.* **2000**, *87*, 7442–7447.
- (69) Dang, N. V.; Dung, N. T.; Phong, P. T.; Lee, I. J. Effect of  $Fe^{3+}$  Substitution on Structural, Optical and Magnetic Properties of Barium Titanate Ceramics. *Phys. B* **2015**, *457*, 103–107.
- (70) Shannon, R. D. Revised Effective Ionic Radii and Systematic Studies of Interatomic Distances in Halides and Chalcogenides. *Acta Crystallogr., Sect. A: Cryst. Phys., Diffr., Theor. Gen. Crystallogr.* **1976**, *A32*, 751–767.
- (71) Malinofsky, W. W.; Kedesdy, H. Barium Iron Oxide Isomorphs of Hexagonal and Tetragonal  $BaTiO_3$ . *J. Am. Chem. Soc.* **1954**, *76*, 3090–3091.
- (72) Zanne, M.; Gleitzer, C. *Bulletin de La Societe Chimique de France* **1971**, 1567.
- (73) Mori, K.; Kamiyama, T.; Kobayashi, H.; Oikawa, K.; Otomo, T.; Ikeda, S. Structural Evidence for the Charge Disproportionation of  $Fe^{4+}$  in  $BaFeO_{3-\delta}$ . *J. Phys. Soc. Jpn.* **2003**, *72*, 2024–2028.
- (74) Liu, S.; Zhang, H.; Sviridov, L.; Huang, L.; Liu, X.; Samson, J.; Akins, D.; Li, J.; O'Brien, S. Comprehensive Dielectric Performance of Bismuth Acceptor Doped  $BaTiO_3$  Based Nanocrystal Thin Film Capacitors. *J. Mater. Chem.* **2012**, *22*, 21862.

- (75) Ezzat, M.; Sabiha, N. A.; Izzularab, M. Accurate Model for Computing Dielectric Constant of Dielectric Nanocomposites. *Appl. Nanosci.* **2014**, *4*, 331–338.
- (76) Lombardi, J.; Pearsall, F.; Li, W.; O'Brien, S. Synthesis and Dielectric Properties of Nanocrystalline Oxide Perovskites,  $[KNbO_3]_{1-x}[BaNi_{0.5}Nb_{0.5}O_{3-\delta}]_x$ , Derived from Potassium Niobate KNbO<sub>3</sub> by Gel Collection. *J. Mater. Chem. C* **2016**, *4*, 7989–7998.
- (77) Mishra, A. Iron-Doped BaTiO<sub>3</sub>: Influence of Iron on Physical Properties. *Int. J. Mater. Sci. Appl.* **2012**, *1*, 14.
- (78) Yang, L.; Qiu, H.; Pan, L.; Guo, Z.; Xu, M.; Yin, J.; Zhao, X. Magnetic Properties of BaTiO<sub>3</sub> and BaTi<sub>1-x</sub>M<sub>x</sub>O<sub>3</sub> (M = Co, Fe) Nanocrystals by Hydrothermal Method. *J. Magn. Magn. Mater.* **2014**, *350*, 1–5.
- (79) Dutta, D. P.; Roy, M.; Maiti, N.; Tyagi, A. K. Phase Evolution in Sonochemically Synthesized Fe<sub>3+</sub> Doped BaTiO<sub>3</sub> Nanocrystallites: Structural, Magnetic and Ferroelectric Characterisation. *Phys. Chem. Chem. Phys.* **2016**, *18*, 9758–9769.
- (80) Khirade, P. P.; Birajdar, S. D.; Raut, A. V.; Jadhav, K. M. Multiferroic Iron Doped BaTiO<sub>3</sub> Nanoceramics Synthesized by Sol-Gel Auto Combustion: Influence of Iron on Physical Properties. *Ceram. Int.* **2016**, *42*, 12441–12451.